Title: Variable susceptibility of intestinal organoid-derived monolayers to SARS-CoV-2 infection

Kyung Ku Jang[1], Maria E Kaczmarek[2#], Simone Dallari[1], Ying-Han Chen[1], Takuya Tada[2], Jordan Axelrad[3], Nathaniel R. Landau[2], Kenneth A Stapleford[2*] and Ken Cadwell[1,2,3*]

[1] Kimmel Center for Biology and Medicine at the Skirball Institute, New York University Grossman School of Medicine, New York, NY, USA

[2] Department of Microbiology, New York University Grossman School of Medicine, New York, NY 10016, USA.

[3] Division of Gastroenterology and Hepatology, Department of Medicine, New York University Grossman School of Medicine, New York, NY 10016, USA.

#Present address: EcoHealth Alliance in New York, NY 10018

*Correspondence:
Ken Cadwell
Email: ken.cadwell@med.nyu.edu
Kenneth Stapleford
Email: kenneth.stapleford@nyulangone.org

ABSTRACT

Gastrointestinal effects associated with COVID-19 are highly variable for reasons that are not understood. In this study, we used intestinal organoid-derived cultures differentiated from primary human specimens as a model to examine inter-individual variability. Infection of intestinal organoids derived from different donors with SARS-CoV-2 resulted in orders of magnitude differences in virus replication in small intestinal and colonic organoid-derived monolayers. Susceptibility to infection correlated with *ACE2* expression level and was independent of donor demographic or clinical features. *ACE2* transcript levels in cell culture matched the amount of ACE2 in primary tissue indicating this feature of the intestinal epithelium is retained in the organoids. Longitudinal transcriptomics of organoid-derived monolayers identified a delayed yet robust interferon signature, the magnitude of which corresponded to the degree of SARS-CoV-2 infection. Interestingly, virus with the Omicron variant spike protein infected the organoids with the highest infectivity, suggesting increased tropism of the virus for intestinal tissue. These results suggest that heterogeneity in SARS-CoV-2 replication in intestinal tissues results from differences in ACE2 levels, which may underlie variable patient outcomes.

MAIN TEXT

Intestinal organoid cultures have transformed our ability to investigate properties of the human intestinal epithelium. Consisting of organized epithelial cell clusters differentiated from somatic stem cells, intestinal organoids generated from endoscopic pinch biopsies are capable of self-renewal and recreate many of the structural, functional, and molecular characteristics of the tissue of origin (1). Investigators have exploited these versatile properties of intestinal organoids to study infectious agents that are otherwise difficult to examine, including viruses such as noroviruses (2-4). Intestinal organoids can also inform our understanding of inter-individual differences in disease susceptibility, such as elucidating the mechanisms by which mutations accumulate in patients with colorectal cancer (5, 6). Additionally, we and others have documented substantial heterogeneity in the growth, morphology, viability, and susceptibility to cytokine toxicity of human intestinal organoid lines (1, 6-8). However, how this heterogeneity relates to resistance of the intestinal epithelium to infectious agents remains unclear.

Although severe acute respiratory syndrome coronavirus 2 (SARS-CoV-2) infection is primarily associated with dysfunction of the respiratory system, the gastrointestinal (GI) tract is also an established target organ in patients with COVID-19. As many as 60% of patients present with diarrhea, vomiting, abdominal pain, anorexia, and/or nausea (9-16). Also, SARS-CoV-2 antigen in intestinal biopsies and viral RNA in the stool are readily detected, even after the virus is undetectable in respiratory samples (17-27). To a limited extent, virions and infectious particles have been detected in patient intestinal and stool specimens (17, 25, 28, 29). Although the pathophysiological significance of these observations has not been resolved, the prolonged presence of viral antigens in the gut is likely to impact antibody evolution (17). Consistent with a potential intestinal tropism, intestinal epithelial cells display robust expression of the SARS-CoV-2 receptor angiotensin I converting enzyme 2 (ACE2) and transmembrane proteases TMPRSS2 and TMPRSS4 that facilitate viral entry (30-32). Further, human intestinal organoids derived from either somatic stem cells or inducible pluripotent stem cells (iPSCs) support SARS-CoV-2 reproduction (32-35). These studies have shown that *ACE2* expression levels can differ based on the differentiation state and anatomical region from which the organoids are derived, but whether this affects the degree of SARS-CoV-2 infection is debated. A broader comparison of gene expression patterns and SARS-CoV-2 infection across organoids from different donors and culture conditions may help interpret the studies that have highlighted the extreme range of *ACE2* expression in intestinal tissues associated with demographic and clinical features of individuals, which could have consequences for susceptibility to both viral infections and inflammatory conditions (36-42).

Only small numbers of independent small intestinal and colonic organoid lines were compared to one another in previous studies examining SARS-CoV-2 infection of intestinal epithelial cells. Thus, the importance of the anatomical origin of organoids and other variables remains unclear. We established and differentiated 3D organoid lines from small intestinal and colonic biopsies procured from 12 and 13 donors, respectively, from healthy donors and patients with inflammatory bowel disease (IBD) of both sexes (Supplemental Table 1). The expression of *ACE2*, *TMPRSS2,* the enterocyte marker of differentiation *APOA1*, and representative interferon stimulated genes (ISGs) *ISG15*, *OASL*, and *MX2* were significantly higher in small intestinal and colonic organoid lines cultured in 3D differentiation media (3DD) compared with those cultured in expansion media (3DE) that maintains organoids in an undifferentiated state (Supplemental Fig. 1A, B, and D-G). *TMPRSS4* expression was similar in both conditions (Supplemental Fig. 1C). Donor-to-donor variability in expression of these genes may reflect the inflammatory environment from which the stem cells were procured. However, 3DE organoids derived from IBD and non-IBD donors displayed comparable gene expression patterns except the decreased *OASL* expression in IBD donor-derived colonic 3DE organoids (Supplemental Fig. 1H). Intestinal organoids can be grown as differentiated monolayers to expose the apical side and facilitate viral entry. We found that the level of *ACE2*, *TMPRSS2*, *TMPRSS4*, *APOA1*, *ISG15*, *OASL*, and *MX2* expression in organoid-derived 2D monolayers correlated well with 3DD organoids generated from the same donor (Fig. 1A-D), suggesting that organoid lines retain their intrinsic gene expression patterns independent of these two culturing conditions. In addition, we found that monolayers exhibited the highest *ACE2* and *TMPRSS2* expression among the culture conditions we examined (Fig. 1E and F) whereas 3DD organoids showed the highest *TMPRSS4*, *APOA1*, *ISG15*, *OASL*, and *MX2* expression (Fig. 1G-K). Therefore, we used the monolayer model to perform all subsequent analyses.

We investigated whether *ACE2*, *TMPRSS2*, or *TMPRSS4* expression differed between small intestinal and colonic organoid-derived monolayers. Although *ACE2* expression did not differ, *TMPRSS*2 and *TMPRSS4* expression were higher and *APOA1* was decreased in colonic monolayers (Supplemental Fig. 1I-L). Five pairs of the small intestinal and colonic organoid lines were generated from the same individual. We found that gene expression patterns were generally the same when comparing small intestinal and colonic monolayers from the same donor (Supplemental Fig 2A). The lack of correlation between *ACE2* or *TMPRSS2* expression and *APOA1* expression suggested that heterogeneous *ACE2* and *TMPRSS2* levels were not an artifact caused by insufficient differentiation (Supplemental Fig. 2B and C). When we segregated the data based on disease status or sex, the only difference we observed was decreased *ACE2*

and *APOA1* expression in colonic monolayers derived from IBD patients compared with non-IBD donors (Supplemental Fig. 2D-F). The expression of *ISG15*, *OASL,* and *MX2* were also not correlated with disease status or sex (Supplemental Fig. 2E and F), although we note that *ISG15* and *OASL* transcripts were higher in colonic versus small intestinal monolayers (Supplemental Fig. 3A and B). These transcripts generally did not correlate with the age of subjects (Supplemental Table 2).

ACE2 expression differed by as much as 5.9-fold when comparing monolayers with the highest and lowest expression of this gene (Fig. 2A). To test whether such differences lead to heterogeneity in viral infection, we infected monolayers with SARS-CoV-2 at a multiplicity of infection (MOI) of 4 for 72 hrs. Remarkably, the amount of virus detected in the supernatant of culture media by plaque assay differed by as much as 423-fold (Fig. 2B). Immunofluorescence microscopy analyses of ACE2 and SARS-CoV-2 nucleoprotein (NP) in representative monolayers confirmed these findings – SI1 and C1 (susceptible small intestinal and colonic monolayers, respectively, with high *ACE2* transcript levels) displayed higher degrees of ACE2 and NP staining compared with SI10 and C8 (resistant small intestinal and colonic monolayers, respectively) (Fig. 2C and D). Indeed, SARS-CoV-2 infection correlated with *ACE2* and *TMRPSS2* expression, but not *TMPRSS4* and *APOA1* expression (Fig. 2E-H). We validated these findings based on relative *ACE2* transcript levels by enumerating absolute RNA copy numbers. The strong correlation between high copy numbers of *ACE2* ($2.9 \times 10^5 – 1.7 \times 10^6$ transcripts/µg of RNA) with SARS-CoV-2 infection supported the relationship between susceptibility to infection and *ACE2* expression (Supplemental Fig 3D). The amount of virus recovered from monolayers were comparable when the data was segregated by the tissue location, the disease status, or sex of the donors (Supplemental Fig. 3E). Similarly, virus production did not correlate with donor age (Supplemental Fig. 3F).

The association between susceptibility to SARS-CoV-2 infection and *ACE2* expression was clear in most cases, but there were outliers for the colonic monolayers. For instance, C7 and C8 have moderate to high levels of ACE2 but low levels of virus production (Fig. 2A and B). Thus, we investigated whether other factors may contribute to differential SARS-CoV-2 infectivity. Several polymorphisms are predicted to alter the stability of ACE2 or alter its affinity to the SARS-CoV-2 spike (S) protein (43-46). However, the sequence of the *ACE2* coding region of C7 and C8 were identical to other donors (Supplemental Table 1). Differences in interferon responses may also contribute to SARS-CoV-2 infectivity, where higher ISG levels are predicted to confer protection against viral infection (47-49). Baseline *ISG15*, *OASL*, and *MX2* expression in C7 and C8 did not explain the lower virus production (Supplemental Fig. 3A-C), and we did not observe

correlations between *ISG15, OASL*, or *MX2* and SARS-CoV-2 susceptibility (Supplemental Fig. 3G-I). Next, we examined ISG expression following stimulation with interferon-beta (IFNβ) or interferon-lambda 2 (IFNλ2). Although we observed varied levels of ISG induction, they were not associated with reduced viral infection (Supplemental Fig. 4A; Supplemental Table 3). Generally, we did not detect an association between the degree to which these ISGs were induced and properties of the donor tissue location, disease status, and age (Supplemental Fig. 4A-C and Supplemental Table 3). However, small intestinal monolayers from female donors displayed higher ISG expression than male donors following IFNλ2 stimulation (Supplemental Fig. 4D). *ACE2* and *TMPRSS2* expression were not altered by IFNβ or IFNλ2 (Supplemental Fig. 5), indicating that *ACE2* and *TMPRSS2* are not ISGs in monolayers. We note that this limited survey of transcript level changes does not rule out a potential role for antiviral cytokines, and a comprehensive protein level analyses of immune mediators will be necessary to identify additional mechanisms of resistance.

Our results thus far are consistent with the possibility that *ACE2* gene expression is a key determinant of the degree to which the intestinal epithelium of an individual is susceptible to SARS-CoV-2 infection. As organoids are differentiated from primary stem cells and expanded in culture (50, 51), it was unclear whether inter-donor differences reflect ACE2 levels in the primary tissues. Therefore, we measured ACE2 protein by immunofluorescence microscopy in small intestinal and colonic sections from the same donors corresponding to individual lines of organoid-derived monolayers (Fig. 3 and Supplemental Fig. 6). ACE2 staining was restricted to the epithelium and most intense along the apical brush boarder (villi in the small intestine and top of the crypts in the colon; Fig. 3A and B and Supplemental Fig. 6A and B), consistent with our data and previous studies showing that *ACE2* expression is enriched in differentiated enterocytes (32, 33). Primary tissue specimens also displayed heterogeneous ACE2 protein levels (Fig. 3C and Supplemental Fig. 6). The ACE2 mean intensity was decreased in colonic sections of IBD patients, but did not differ when comparing tissue location or sex (Fig 3D). The mean intensity of ACE2 staining in intestinal tissue sections strongly correlated with *ACE2* transcript and SARS-CoV-2 levels in monolayers derived from the same individual, and not with age, sex, or disease status (Fig. 3E). Therefore, organoid-derived monolayers retain the variable ACE2 levels from its original tissue.

To further investigate how susceptible and resistant organoids differ from each other, we selected the three colonic monolayer lines that each displayed high infection (HI; C1, C2, and C3) or low infection (LI; C8, C12, and C13) for RNA-seq analysis. We validated the transcriptional and microscopy analyses (Fig. 2A, C, and D) by Western blot, which showed higher levels of ACE2

protein in HI compared with LI monolayers, and comparable levels of TMPRSS2 protein (Fig. 4A). We then infected the monolayers with SARS-CoV-2 for 24 and 72 hrs (I24 and I72, respectively), and compared these samples with mock infected monolayers harvested at 0 and 72 hrs (UI0 and UI72, respectively). SARS-CoV-2 continues to replicate in organoids after the initial 24 hrs, likely due to the low proportion of cells that are initially infected (33). We reasoned sampling early and late time points may distinguish transcriptional changes that contribute to resistance and susceptibility to infection versus those that are a consequence. Because these six monolayer lines were prepared from independently thawed batches of frozen organoid stocks, we quantified virus and confirmed that higher amounts of SARS-CoV-2 were recovered from HI compared with LI monolayers at both time points (Fig. 4B and C). Both HI and LI monolayers remained viable following SARS-CoV-2 infection (Supplemental Fig. 7A). Similar to our findings with IFN-stimulated monolayers (Supplemental Fig. 5), *ACE2* and *TMPRSS2* transcripts in both HI and LI monolayers were stable during the course of infection (Supplemental Fig. 7B and C).

The number of transcripts displaying > 2-fold changes (adjusted *P*-value < 0.05) in 12 pairwise comparisons are summarized in Supplemental Fig. 7D. The conditions that displayed the most differences from one another were those comparing early time points to 72 hrs post-infection. Uninfected samples at 0 and 72 hrs displayed no differences, indicating that the transcriptome of uninfected HI and LI monolayers remained stable over time. This result increased our confidence that monolayers were fully differentiated at the onset of our experiments. Also, few genes displayed differential expression when comparing uninfected HI and LI monolayers. Principal component analysis (PCA) showed that infection at 72 hrs separated samples on PC1 and susceptibility to infection (HI versus LI) separated samples on PC2 (Supplemental Fig. 7E). PCA also confirmed observations from the pairwise comparison indicating that uninfected monolayers and those infected for 24 hrs were transcriptionally similar.

At the 72 hr time point, where the largest transcriptional changes occurred between conditions, we found that the majority of the differentially expressed genes (DEGs) when comparing uninfected and infected conditions (55 of 71) were common to LI and HI monolayers, while most DEGs (65 of 81) when comparing infected HI and LI monolayers were unique to this comparison (Fig. 4D). Gene ontology analyses and Ingenuity Pathway Analysis (IPA) showed that SARS-CoV-2 infection impacts antiviral pathways, especially those related to the interferon response, and that this signature was more pronounced in HI monolayers compared with LI monolayers following infection (Fig. 4E-G and Supplemental Fig. 7F). Indeed, differentially expressed genes related to the *response to type I IFN* (*SAMHD1*, *NLRC5*, *USP18*, *IFIT1*, *ZBP1*, *SHFL*, *STAT2*, *IRF7*, *SP100*, *MX1*, *OAS3*, *STAT1*, *ISG15*, and *OAS2*) and *JAK-STAT* (*STAT5A*,

STAT1, *STAT2*, *CCL2*, and *NMI*) included common ISGs, and although these were upregulated in both HI and LI monolayers infected by SARS-CoV-2, they were induced to a higher degree in HI monolayers (Supplement Fig. 7G and H). Because these ISGs are more highly expressed in HI monolayers and not detected at 24 hrs, they are likely a response to the increased degree of infection. These results are consistent with other studies suggesting that the interferon response to SARS-CoV-2 is delayed (33, 49, 52, 53). Unexpectedly, multiple genes associated with pathways related to zinc and copper homeostasis were specifically upregulated in LI compared to HI monolayers after 72 hrs of infection (Fig 4E, H and Supplemental Fig. 7I). The increased expression of *MT1* genes encoding metallothionines in LI monolayers was particularly striking and may be indicative of a stress response activated by viral perturbations in the epithelium (54, 55). Collectively, longitudinal transcriptome analyses identified robust yet late transcriptional changes induced by SARS-CoV-2, the magnitude of which corresponded to the levels of viral infection.

The transcriptome analysis did not provide additional insight into the difference in *ACE2* between expression displayed by HI and LI monolayers. The transcription factors BRG1, FOXM1, and FOXA2 mediate *ACE2* expression (56, 57) but consistent with the RNA-Seq results, HI and LI monolayers displayed comparable *BRG1*, *FOXM1*, and *FOXA2* expression by qPCR (Supplemental Fig. 8A-C). However, we detected increased protein levels of FOXA2 in HI monolayers by Western blot, suggesting a probable mechanism for the high *ACE2* expression observed in these donors (Supplemental Fig. 8D).

During the preparation of this manuscript, a new variant of concern designated as Omicron emerged with multiple amino acid substitutions in the S protein. Thus, we examined the ability of the Omicron S protein to mediate entry into intestinal epithelial cells using SARS-CoV-2 S protein-pseudotyped lentiviral reporter viruses (58). Vesicular stomatitis virus G protein (VSV-G) pseudotyped control virus displayed high infectivity of organoid-derived monolayers demonstrating feasibility of this approach (Supplemental Fig. 9A). Although Omicron S protein has been observed to have weaker or comparable binding affinity to ACE2 (59, 60), Omicron S protein pseudotyped virus displayed 2.5- and 5-fold higher infection than Delta and D614G pseudotypes, respectively (Supplemental Fig. 9A), suggesting that Omicron exploits different or additional cell entry pathways to replicate in human intestinal organoids. Consistent with our observation, a recent study showed efficient entry of Omicron using the endosomal route (61). D614G and Omicron S protein pseudotyped viruses showed 1.2- to 1.3-fold higher infection of HI monolayers compared with LI monolayers whereas the Delta S protein pseudotyped virus displayed comparable infectivity (Supplemental Fig. 9B). This marginal contribution of the

differential *ACE2* expression to infection of these pseudotyped viruses suggests that other factors may be involved in SARS-CoV-2 susceptibility of intestinal epithelial cells. For example, *MT1* genes identified in our RNA-Seq experiment (Fig. 4E and H) are associated with resistance to hepatitis C virus and human cytomegalovirus, and zinc ion suppresses the SARS-CoV-2 replications by inhibiting its main proteases (62-65). Although we caution against overinterpreting these results obtained with pseudotyped viruses, we believe these preliminary results justify future studies using intestinal organoids and other donor-derived cell culture systems to examine differential susceptibility to intact viruses representing existing and future variants.

When taken together, our results show that human intestinal organoids reveal interindividual differences in responses to viral infection. Organoid-derived monolayers showed substantial differences in their susceptibility to SARS-CoV-2 infection, and ACE2 levels were the strongest correlate of susceptibility. Although transcriptome analysis identified many differentially expressed genes upon SARS-CoV-2 infection when comparing organoid lines, these differences were not apparent at 24 hrs post-infection, a time point at which the degree of virus infection already diverged between resistant and susceptible monolayers. Therefore, these gene expression patterns are unlikely to account for differential susceptibility, and instead, provide a glimpse as to how increased viral replication can affect properties of the intestinal epithelium. Although the presence of SARS-CoV-2 RNA in the gut has been associated with diarrhea in patients with COVID-19 (27), the consequence of intestinal epithelial infection remains largely unclear and an important area of investigation. Extensive experiments in animal models predict that activation of viral RNA sensors trigger immune responses including ISGs that impact the intestinal barrier (66-76). Co-culturing organoids with leukocytes may help our understanding of the downstream consequences of epithelial infections (7). Additionally, loss of microbiome diversity is associated with COVID-19 severity (77-80). It would be important to determine whether the microbiome is involved in infection of the epithelium or represents an independent variable of disease outcome.

Finally, it is notable that organoids retained the differential ACE2 levels observed in intact primary tissue sections from the same donor. These results indicate that at least some transcriptional properties of the original intestinal epithelium that are individual-specific are retained following *ex vivo* differentiation. If this finding is generalizable, then organoids can be a powerful platform to investigate interindividual differences in infectious disease susceptibility.

METHODS

Human intestinal tissue specimen collection:

Patients with and without IBD were recruited at outpatient colonoscopy performed for colon cancer screening, surveillance, or IBD activity assessment at NYU Langone Health's Ambulatory Care Center, New York, under an NYU Grossman School of Medicine Institutional Review Board–approved study (Mucosal Immune Profiling in Patients with Inflammatory Bowel Disease; S12-01137). Approximately 6 pinch biopsies were obtained from the ascending colon of each patient using a 2.8-mm standard endoscopic biopsy forceps. The inflammation status of tissue was confirmed by endoscopic and histopathological examination. All pinch biopsies were collected in ice-cold complete RPMI (RPMI 1640 medium supplemented with 10% fetal bovine serum (FBS), penicillin/streptomycin/glutamine, and 50 μM 2-mercaptoethanol). Pinch biopsies were then transferred to freezing media (90% FBS + 10% DMSO) in Cryogenic Tubes and stored in liquid nitrogen.

Culture of human small intestinal and colonic organoids:

Human organoids were cultured as described previously (7, 68). Pinch biopsies were thawed in PBS and then incubated in Gentle Cell Dissociation Reagent (Stemcell Technologies) on ice for 30 min, followed by vigorous pipetting to isolate crypts. The crypts were embedded in 30 μl of Matrigel and cultured with Human IntestiCult™ Organoid Growth Medium (OGM) (Basal Medium and Organoid Supplement, Stemcell Technologies) supplemented with 100 IU Penicillin and 100 μg/ml Streptomycin (Corning) and 125 μg/ml Gentamicin (ThermoFisher), herein referred to as expansion medium. The culture medium was changed every 2-3 days. For passaging human organoids, 10 μM Y-27632 were added for the first 2 days. For differentiation, the human organoids were cultured with 1:1 mix of Human IntestiCult™ OGM Basal Medium and DMEM/F-12 (ThermoFisher) in the presence of 100 IU Penicillin and 100 μg/ml Streptomycin, 125 μg/ml Gentamicin and 2 mM L-Glutamine (Corning), herein referred to as differentiation medium. To generate organoid-derived monolayers, mature human small intestinal colonic organoids grown with the expansion media were digested into single cells using TrypLE Express (ThermoFisher) and seeded into Matrigel-coated 96-well culture plate (Corning) in Y-27632-supplemented expansion medium at 150,000 cells/well for the first 2 days. The culture media were changed every day. In experiments in which organoids were treated with recombinant interferons, monolayers grown with the differentiation media for 7 days were stimulated with human IFNβ (100 or 300 IU/ml, R&D systems) or IFNλ2 (10 or 30 ng/ml, R&D systems) for 12 hrs.

Transcript analysis:

Total RNA was extracted from human organoids using RNeasy Mini Kit with DNase treatment (QIAGEN), and synthesis of cDNA was conducted with High-Capacity cDNA Reverse Transcription Kit (ThermoFisher) according to the manufacturer's protocol. RT-PCR was performed using SybrGreen (Roche) on a Roch480II Lightcycler using the following primers: *ACE2*, Fwd 5'-TCAAGGAGGCCGAGAAGTTC-3' and Rev 5'-TTCCTGGGTCCGTTAGCATG-3'; *TMPRSS2*, Fwd 5'-ACCTGATCACACCAGCCATG-3' and Rev 5'-CTTCGAAGTGACCAGAGGCC-3'; *TMPRSS4*, Fwd 5'-CCGATGTGTTCAACTGGAAG-3' and Rev 5'-GAGAAAGTGAGTGGGAACTG-3'; *APOA1*, Fwd 5'-TGGATGTGCTCAAAGACAGC-3' and Rev 5'-AGGCCCTCTGTCTCCTTTTC-3'; *ISG15*, Fwd 5'-GAGAGGCAGCGAACTCATCT-3' and Rev 5'-CTTCAGCTCTGACACCGACA-3'; *OASL*, Fwd 5'-AAAGAGAGGCCCATCATCC-3' and Rev 5'-ATCTGGGTAACCCCTCTG C-3'; *MX2*, Fwd 5'-CAGCCACCACCAGGAAACA-3' and Rev 5'-TTCTGCTCGTACTGGCTGTACAG-3'; BRG1, Fwd 5'-AGTGCTGCTGTTCTGCCAAAT-3' and Rev 5'-GGCTCGTTGAAGGTTTTCAG-3'; FOXM1, Fwd 5'-GCAGGCTGCACTATCAACAA-3' and Rev 5'-TCGAAGGCTCCTCAACCTTA-3'; FOXA2, Fwd 5'-GGGAGCGGTGAAGATGGA-3' and Rev 5'-TCATGTTGCTCACGGAGGAGTA-3'; *GAPDH*, Fwd 5'-GATGGGATTTCCATTGAT GACA-3' and Rev 5'-CCACCCATGGCAAATTCC-3'; ACTB, Fwd 5'-CCCAGCCATGTACGTTGCTA-3' and Rev 5'-TCACCGGAGTCCATCACGAT-3'; SARS-CoV-2 NP, Fwd 5'- ATGCTGCAATCGTGCTACAA-3'; SARS-CoV-2 N, Rev 5'-GACTGCCGCCTCTGCTC-3'. The expression of the respective genes was normalized by geometric mean of *GAPDH* and *ACTB* expression with $\Delta\Delta C_T$ method (81). Where indicated, the values were expressed as fold change from uninfected or untreated organoids. To determine the copy number of *ACE2* mRNA, a standard curve was constructed with the range of 1.4×10^5 to 9.4×10^9 molecules of hACE2 (Plasmid #1786, Addgene) (82) in which *ACE2* transcripts showed optimal PCR efficiencies. The copy number of *ACE2* transcripts in the organoids was calculated from the linear regression of the standard curve and normalized with the RNA input.

Virus infection and plaque assay:

SARS-CoV-2 infection experiments were performed in the ABSL3 facility of NYU Grossman School of Medicine in accordance with its Biosafety Manual and Standard Operating Procedures. The organoid monolayers grown with the differentiation media for 7 days were infected with icSARS-CoV-2-mNG (isolate USA/WA/1/2020) obtained from the UTMB World Reference Center for Emerging Viruses and Arboviruses (83). A working stock of SARS-CoV-2-mNG was generated by infecting a 90-95% confluent monolayer of Vero E6 cells (ATCC CRL-

1586) for 48 hrs at 37°C. Following incubation, the supernatant was collected, centrifuged at 1,200 rpm for 5 mins, aliquoted and stored at -80°C. Viral titers were quantified by plaque assay as described below. For the infection, organoid monolayers were infected with SARS-CoV-2-mNG at a MOI of 4 for 1 hr at 37°C. Following incubation, organoids were washed 4 times with phosphate buffered saline (PBS) and differentiation media was added for the indicated time. Total virus in the 3rd or 4th wash was also quantified to ensure excess virus was removed. Thus, virus quantified at the end of the experiment can be assessed as replicative particles rather than residual particles persisting in culture. Viral titers in the monolayer supernatants were quantified by plaque assay.

To quantify infectious virus by plaque assay, 10-fold serial dilutions of each sample were made in Dulbecco's Modified Eagle Medium (DMEM). Each dilution was added to a monolayer of Vero E6 cells for 1 hr at 37°C. Following incubation, DMEM supplemented with 2% fetal bovine serum and 0.8% agarose was added and the incubated for 72 hrs at 37°C. Cells were then fixed with 10% formalin, the agarose plug removed, and wells stained with crystal violet (10% crystal violet, 20% ethanol). Virus titers (PFU/ml) were determined by counting the number of plaques on the lowest countable dilution.

For thiazolyl blue tetrazolium bromide (MTT) reduction assay, staining with MTT was adapted from a previously described method (7). Briefly, we added MTT (Sigma-Aldrich) into the monolayers to a final concentration of 500 µg/ml on 72 hrs post-infection. After incubation for 2 hrs at 37°C, 5% CO_2, the medium was discarded and 20 µl of 2% SDS (Sigma-Aldrich) solution in water was added to solubilize the Matrigel for 2 hrs. Then, 100 µl of DMSO (ThermoFisher) was added for 1 hr to solubilize the reduced MTT, and OD was measured on a microplate absorbance reader (ParkinElmer) at 562 nm. The specific organoid death (%) was calculated as MTT deduction (%) by normalizing to uninfected monolayers which were defined as 100% viable.

***ACE2* sequencing:**

A 2418-bp region containing the *ACE2* coding region was amplified from cDNA prepared from organoids (see above) by PCR using a pair of primers (Fwd 5'-ATGTCAAGCTCTTCCTGGCTCC-3' and Rev 5'-CTAAAAGGAGGTCTGAACATCATCAGTG-3'). Amplicons were cloned into pCR™2.1-TOPO® (Invitrogen). The plasmids were sequenced by Sanger sequencing from Psomagen using 4 primers: M13F, 5'-GTAAAACGACGGCCAGT-3'; M13R, 5'-CAGGAAACAGCTATGAC-3'; ACE2_600F, 5'- GGGGATTATTGGAGAGGAGACT-3'; ACE2_1800R, 5'- GTCGGTACTCCATCCCACA-3'.

Immunofluorescence:

ACE2 staining were performed as described previously (84). Briefly, pinch biopsies of the terminal ileum and ascending colon were fixed in 10% formalin and embedded in paraffin blocks. Sections were cut to 5 µm thickness at the NYU Center for Biospecimen Research and Development and mounted on frosted glass slides. For deparaffinization, slides were baked at 70°C for 1.5 h, followed by rehydration in descending concentration of ethanol (100%, 95%, 80%, 70%, ddH_2O twice; each step for 30 s). HIER was performed in a pressure cooker (Biocare Medical) using Dako Target Retrieval Solution, pH 9 (Dako Agilent) at 97°C from 10 min and cooled down to 65°C. After further cooling to room temperature for 20 min, slides were washed for 10 min 3 times in Tris-Buffered Saline (TBS), containing 0.1% Tween 20 (Sigma; TBS-T). Sections were blocked in 5% normal donkey serum (Sigma) in TBS-T at room temperature (RT) for 1 hr, followed by incubation with rabbit anti-ACE2 antibody (1:100, Abcam, ab15348) in the blocking solution at 4°C overnight. Sections were washed 3 times with TBS-T and stained with the Alexa Flour 555 conjugated with donkey anti-rabbit IgG (1:500, ThermoFisher, A-31572) in PBS with 3% bovine serum albumin (BSA) (ThermoFisher), 0.4% saponin, and 0.02% sodium azide at RT for 1 hr. Following this, sections were washed 3 times with TBS-T and mounted with ProLong™ Glass Antifade Mountant with NucBlue™ Stain (ThermoFisher, P36918). Images were acquired using an EVOS FL Auto Cell Imaging System (ThermoFisher) and then processed and quantified using ImageJ.

SARS-CoV-2-infected monolayers were fixed with 4% paraformaldehyde (Electron Microscopy Sciences) for 3 hrs at RT. Following fixation, cells were washed 3 times with PBS then blocked and permeabilized in PBS with 0.1% Triton-X100 and 3% BSA for 0.5 hr at RT. The permeabilized organoids were washed 3 times with PBS and incubated with mouse anti-SARS-CoV-2 N antibody (1:1,000, ProSci, 10-605) and rabbit anti-ACE2 antibody (1:500, Abcam, ab15348) diluted in PBS containing 3% BSA overnight at 4°C. The monolayers were washed 3 times with PBS and stained with Alexa Flour 647 conjugated with goat anti mouse IgG (1:2,000, ThermoFisher, A32728) and Alexa Flour 594 conjugated with donkey anti rabbit IgG (1:1,000, ThermoFisher, 21207) diluted in PBS with 3% BSA and 4'6-diamidino-2-phenylindole (DAPI) for 1 hr at RT. The monolayers were then washed 3 times with PBS and imaged using the CellInsight CX7 High-content Microscope (ThermoFisher).

Immunoblotting:

Organoids were processed for immunoblotting as previously described (76). Briefly, monolayers were incubated in lysis buffer (20 mM Tris-HCl (pH 7.4), 150 mM NaCl, 1% Triton X-100, 10%

glycerol, and 2x Halt Protease and Phosphatase Inhibitor Cocktail (ThermoFisher) on ice for 5 min and centrifuged at 14,000 rpm for 20 min. Samples were resolved on Bolt 4-12% Bis-Tris Plus Gels (Invitrogen), transferred onto PVDF membranes, and blocked using 5% skim milk. The following antibodies were used for immunoblotting studies: mouse anti-β-actin (1:5,000, Sigma, AC-15), rabbit anti-ACE2 (1:1,000, Abcam, ab15348), mouse anti-TMPRSS2 (1:1,000, Santa Cruz, sc-515727), rabbit anti-BRG1 (1:250, R&D systems, MAB5738), mouse anti-FOXM1 (1:100, Santa Cruz, sc-271746), rabbit anti-FOXA2 (1:200, Cell Signaling Technology, 8186). Secondary antibodies (mouse anti-rabbit and goat-anti mouse, 211-032-171 and 115-035-174, respectively) were purchased from JacksonImmunoResearch

RNA deep sequencing and analysis:

Monolayers were cultured in differentiation media for 7 days and then were infected with SARS-CoV-2 at MOI of 4 for 24 hrs or 72 hrs before RNA extraction with 2-3 technical duplicates per line. CEL-seq2 was performed on 53 human organoids RNA samples. Sequencing was performed on Illumina NovaSeq 6000 (Illumina). RNA-seq results were processed using the R package “DESeq2” to obtain variance stabilized count reads, fold changes relative to specific condition, and statistical *P*-value. Analysis of the organoid transcriptome focused on differentially expressed genes, defined as the genes with an absolute fold change relative to specific condition >2 and an adjusted *P*-value < 0.05.

Plasmids

SARS-CoV-2 S expression vectors have been previously described (58). Briefly, the SARS-CoV-2 S expression vector pcCoV2.S.Δ19, *S* gene was amplified from pcCOV2.S (Wuhan-Hu-1/2019 SARS-CoV-2 isolate) (58) with a forward primer containing Kpn-I site and reverse primer that deleted the 19 carboxy-terminal amino acids and contained Xho-I site. The amplicon was then cloned into the Kpn-I and Xho-I of pcDNA6 (invitrogen). The D614G mutation was introduced by overlap extension PCR of the Δ19.*S* gene using internal primers overlapping the D614G mutation and cloned into pcDNA6. Mutations in Delta variant S were introduced by overlapping PCR overlapping each Delta mutations and cloned into pcDNA6. The Omicron S expression vector was chemically synthesized and cloned into pcDNA6 (85). pcVSV-G, pLenti.GFP.NLuc, lentiviral packaging plasmids pMDL and pRSV.Rev have been previously described (58).

SARS-CoV-2 S lentiviral pseudotypes

SARS-CoV-2 variant S protein pseudotyped lentiviral stocks were generated by cotransfection of 293T cells (4 X 10^6) with pMDL, pLenti.GFP-NLuc, pcCoV2.S.Δ19 and pRSV.Rev (4:3:4:1 mass ratio) by calcium phosphate coprecipitation as previously described (58). VSV-G pseudotyped lentivirus was generated substituting the S protein vector for pcVSV-G. Two days post-transfection, supernatant was harvested and passed through a 0.45 μm filter and ultracentrifuged over a 20% sucrose cushion at 30,000 RPM for 90 min. The virus pellet was resuspended to 1/10 the initial volume in DMEM with 10% FBS and virus titers were normalized by real-time PCR reverse transcriptase activity. Pseudotyped virus infectivity assay was done with HI and LI monolayers at an MOI of 0.2. After 72 hrs of infection, luciferase activity was measured by Nano-Glo luciferase substrate (Promega) with an Envision 2103 microplate luminometer (PerkinElmer).

Computational and statistical analysis

Gene ontology analysis was performed using the R package “clusterProfiler”. Principal Component Analysis was performed using the R package “stats”. Heatmaps were generated using the R package “pheatmap”. Upstream regulators analysis was performed by uploading the differentially expressed genes to Ingenuity Pathway Analysis software (Qiagen). Statistical differences were determined as described in figure legend using either R or GraphPad Prism 9 software (La Jolla, CA, USA).

Data availability

The accession number for the gene expression raw data reported in this paper is GSE179949.

FUNDING

This research was supported by NIH grants DK093668 (K.C.), AI121244 (K.C.), HL123340 (K.C.), AI130945 (K.C.), AI140754 (K.C.), DK124336 (K.C.), DA046100 (N.R.L), AI122390 (N.R.L), and AI120898 (N.R.L) and a pilot award from the NYU CTSA grant UL1TR001445 from the National Center for Advancing Translational Sciences (NCATS) (K.C.). Additional support was provided by the Faculty Scholar grant from the Howard Hughes Medical Institute (K.C.), Crohn's & Colitis Foundation (K.C.), Kenneth Rainin Foundation (K.C.), Judith & Stewart Colton Center of Autoimmunity (K.C.). K.C. is a Burroughs Wellcome Fund Investigator in the Pathogenesis of Infectious Diseases. M.E.K was supported by a Public Health Service Institutional Research Training Award T32 AI7647.

DECLARATION OF INTERESTS

K.C. has received research support from Pfizer, Takeda, Pacific Biosciences, Genentech, and Abbvie. K.C. has consulted for or received an honoraria from Puretech Health, Genentech, and Abbvie. K.C. holds U.S. patent 10,722,600 and provisional patent 62/935,035 and 63/157,225.

ACKNOWLEDGMENTS

We wish to thank the NYU Grossman School of Medicine Center for Biospecimen Research and Development, Office of Science & Research High-Containment Laboratories, and Flow Cytometry and Cell Sorting, Microscopy, Genome Technology, and Histology Cores (supported by National Institutes of Health [NIH] grants P31CA016087, S10OD01058, and S10OD018338) for their support in the completion of this research and Dr. Meike Dittmann at the NYU Grossman School of Medicine for use of the CX7 CellInsight high-content microscope.

AUTHOR CONTRIBUTION

Conceptualization: Kyung Ku Jang, Kenneth Stapleford, Ken Cadwell
Data curation: Kyung Ku Jang, Kenneth Stapleford, Ken Cadwell
Formal analysis: Kyung Ku Jang, Maria E Kaczmarek, Ying-Han Chen, Simone Dallari
Funding acquisition: Kenneth Stapleford, Ken Cadwell
Investigation: Kyung Ku Jang, Maria E Kaczmarek, Ying-Han Chen, Simone Dallari, Takuya Tada, Kenneth Stapleford
Methodology: Kyung Ku Jang, Maria E Kaczmarek, Ying-Han Chen, Simone Dallari, Takuya Tada, Kenneth Stapleford
Project administration: Kenneth Stapleford, Ken Cadwell
Resources: Kyung Ku Jang, Maria E Kaczmarek, Ying-Han Chen, Simone Dallari, Jordan Axelrad, Nathaniel R. Landau
Supervision: Kenneth Stapleford, Ken Cadwell
Validation: Kyung Ku Jang, Maria E Kaczmarek, Ying-Han Chen, Simone Dallari
Visualization: Kyung Ku Jang, Maria E Kaczmarek, Simone Dallari
Writing – original draft: Kyung Ku Jang, Simone Dallari, Jordan Axelrad, Takuya Tada, Nathaniel R. Landau, Kenneth Stapleford, Ken Cadwell
Writing – review & editing: Kyung Ku Jang, Maria E Kaczmarek, Ying-Han Chen, Simone Dallari, Takuya Tada, Jordan Axelrad, Nathaniel R. Landau, Kenneth Stapleford, Ken Cadwell

Figure 1. Heterogeneous gene expression patterns in small intestinal and colonic organoids.

(A-D) Correlation analysis of *ACE2* and *TMPRSS2* (A), *TMPRSS4* and *APOA1* (B), *ISG15* and *OASL* (C), or *MX2* (D) expression in human intestinal (circle) and colonic (rectangle) organoids cultured as monolayers grown in differentiation media for 7 days with those cultured as human 3D organoids grown in differentiation media (3DD) for 7 days. **(E-K)** RT-PCR data comparing *ACE2* (E), *TMPRSS2* (F), *TMPRSS4* (G), *APOA1* (H), *ISG15* (I), *OASL* (J), and *MX2* (K) expression in human 3D organoids grown with expansion media (3DE), 3DD, and monolayers grown in differentiation media for 7 days. Data points are mean of at least 2 technical replicates of individual organoid lines. Bars represent mean ± SEM, and at least 2 independent experiments were performed. r, Pearson correlation coefficient. $^{**}P \leq 0.01$, $^{***}P \leq 0.001$, and $^{****}P \leq 0.0001$ by simple regression analysis in A-D and paired *t* test, two tailed in E-K.

Figure 2. Differential susceptibility of intestinal organoid-derived monolayers correlates with *ACE2* and *TMPRSS2* expression.

(A) RT-PCR analysis of *ACE2* expression in small intestinal (SI1-SI12) and colonic (C1-C13) monolayers. **(B)** Plaque forming units (PFU) determined by virus titration on Vero E6 cells of supernatant from monolayers at 72 hrs post-infection with SARS-CoV-2. **(C)** Representative immunofluorescence microscopy images showing co-staining of DAPI (blue), ACE2 (green), and SARS-CoV-2 nucleoprotein (NP) (red) in SARS-CoV-2 infected SI1, SI10, C1, and C8 monolayer lines. An image of uninfected C1 is shown as a representative uninfected condition and a Matrigel-coated well without cells is shown as a control for background fluorescence. **(D)** Total intensity of NP and ACE2 normalized with cell counts of SI1, SI10, C1 and C8. **(E-H)** Correlation of SARS-CoV-2 PFU with *ACE2* (E), *TMPRSS2* (F), *TMPRSS4* (G), or *APOA1* (H) expression among monolayers. Data points in A, B, and D are each technical replicate, and data points in E-H are the mean of at least 2 technical replicates of individual organoid lines. Bars represent mean ± SEM, and at least 2 independent experiments were performed. r, Pearson correlation coefficient. $^{*}P \leq 0.05$, $^{**}P \leq 0.01$, $^{***}P \leq 0.001$, and $^{****}P \leq 0.0001$ by simple regression analysis in E-H.

Figure 3. Differential *ACE2* expression observed in individual intestinal organoid lines are conserved in primary tissue from the same donor.

(A and B) Representative ACE2 staining images in primary tissues of terminal ileum (A) and ascending colon (B) from which SI1, SI10, C1, and C13 organoids were established. **(C)** Mean intensity of ACE2 per area (right) in each field of view from the primary tissues from which small

intestinal and colonic organoids were established. **(D)** Mean intensity of ACE2 by disease (left) or sex (right). **(E)** Correlation of ACE2 mean intensity with *ACE2* expressions (left) and SARS-CoV-2 PFU (middle) among monolayers or subject age (right). Data points in C are the field of views, and data points in D and E are mean of at least 2 technical replicates of individual organoid lines. Bars represent mean ± SEM, and at least 2 independent experiments were performed. Bars: 200 μm. SI, small intestine; r, Pearson correlation coefficient. *$P \leq 0.05$, **$P \leq 0.01$, ***$P \leq 0.001$, and ****$P \leq 0.0001$ by unpaired *t* test, two-tailed in D and simple regression analysis in E.

Figure 4. Transcriptome analysis reveals a heighted and delayed interferon response to SARS-CoV-2 infection in susceptible organoid-derived monolayers.

(A) Western blot analysis of ACE2, TMPRSS2, and ACTB in high infection (HI; C1, C2, and C3) and low infection (LI; C8, C12, and C13) lines. Blots are representative of at least 3 independent repeats. **(B)** PFU determined by virus titration on Vero E6 cells of supernatant of HI and LI monolayers at 24 and 72 hrs after infection with SARS-CoV-2. **(C)** RT-PCR analysis of SARS-CoV-2 expression in HI and LI monolayers upon 24 and 72 hrs infection with SARS-CoV-2. **(D)** Venn diagram depicting the number and overlap of differentially expressed genes (DEGs) according to RNA-Seq analysis (see Supplemental Fig. 7) of HI or LI monolayers infected with SARS-CoV-2 for 72 hrs. **(E)** Highly enriched biological process GO terms for the DEGs in HI and LI infected with SARS-CoV-2. **(F and G)** Ingenuity pathway analysis (IPA) of the transcriptome of SARS-CoV-2-infected HI or LI for upstream regulators. Interferon-related genes (F) or Top 5 molecules within the classes *cytokine, transcription regulator, transmembrane receptor, ligand-dependent nuclear receptor, and others* (G) commonly associated with HI infected/uninfected and LI infected/uninfected conditions. **(H)** DEGs of LI infected/HI infected condition were analyzed by IPA for upstream regulators. Top 5 upstream regulators related to Zn ion homeostasis and interferons for the LI. Data points in B and C represent the mean of at least 2 technical replicates of individual organoids lines. Bars represent mean ± SEM, and at least 2 independent experiments were performed. *$P \leq 0.05$, and **$P \leq 0.01$, by unpaired *t* test, two-tailed in B and C.

Supplemental figure 1. Transcriptional analysis in small intestinal and colonic organoids cultured in different media conditions.

(A-D) RT-PCR analysis of *ACE2* (A), *TMPRSS2* (B), *TMPRSS4* (C), *APOA1* (D), *ISG15* (E), *OASL* (F), and *MX2* (G) expression among small intestinal (SI) or colonic 3D organoids grown in expansion media (3DE) or differentiation media (3DD) for 7 days. **(H)** RT-PCR data showing *ACE2*, *TMPRSS2*, *TMPRSS4*, *APOA*, *ISG15*, *OASL*, and *MX2* expression in 3DE organoids

according to disease status. **(I-L)** RT-PCR analysis of *ACE2* (I), *TMPRSS2* (J), *TMPRSS4* (K), and *APOA1* (L) expression among SI and colonic monolayers grown in differentiation media for 7 days. Data points are mean of 3 technical replicates of individual organoid lines. Bars represent mean, and at least 2 independent experiments were performed. SI, small intestine. $^{**}P \leq 0.01$, $^{***}P \leq 0.001$, and $^{****}P \leq 0.0001$ by paired *t* test, two-tailed in A-G and unpaired *t* test, two-tailed in H-L.

Supplemental figure 2. Transcript analysis of organoid-derived monolayers according to tissue location, disease, and sex of subjects.

(A) RT-PCR analysis of *ACE2*, *TMPRSS2*, *TMPRSS4*, *APOA1*, *ISG15*, *OASL*, and *MX2* expression between matched donor-derived small intestinal (SI) and colonic monolayers grown in differentiation media for 7 days. Data is displayed fold-change differences between the expression of the indicated genes in colonic monolayers over expression in SI monolayers **(B and C)** Correlation of *ACE2* (B) and *TMPRSS2* (C) expression with *APOA1* expression among monolayers grown in differentiation media. **(D)** RT-PCR analysis of *ACE2* expression among monolayers grown in differentiation media according to the disease status or sex of subjects. **(E and F)** RT-PCR data depicting *ACE2*, *TMPRSS2*, *TMPRSS4*, *APOA1*, *ISG15*, *OASL*, and *MX2* expression of monolayers according to disease (E) or sex (F). Data points are mean of at least 2 technical replicates of individual organoid lines. Bars represent mean ± SEM, and at least 2 independent experiments were performed. FC, fold change; SI, small intestine; r, Pearson correlation coefficient. $^{*}P \leq 0.05$, $^{**}P \leq 0.01$, and $^{***}P \leq 0.001$ by paired *t* test, two-tailed in A, simple regression analysis in B and C, and unpaired *t* test, two-tailed in D-F.

Supplemental figure 3. Analysis of gene expression and viral replication in organoids by intestinal region, disease, sex, or age of subjects.

(A-C) RT-PCR analysis of *ISG15* (A), *OASL* (B), and *MX2* (C) expression in monolayers. **(D)** Correlation of ACE2 coly number with ACE2 expression (left) or PFU of SARS-CoV-2 (right). **(E)** PFU of SARS-CoV-2 according to intestinal region (left), disease (middle), or sex (right) of subjects. **(F-I)** Correlation of PFU of SARS-CoV-2 with age of subjects (F) or *ISG15* (G), *OASL* (H), and *MX2* (I) expression. Data points are mean of at least 2 technical replicates of individual organoid lines. Bars represent mean ± SEM, and at least 2 independent experiments were performed. SI, small intestine; r, Pearson correlation coefficient. $^{*}P \leq 0.05$, $^{**}P \leq 0.01$, $^{***}P \leq 0.001$, and $^{****}P \leq 0.0001$ by unpaired *t* test, two-tailed in A-C and E and simple regression analysis in D and F-I.

Supplemental figure 4. Transcript analysis of IFNβ- or IFNλ2-stimulated organoids according to intestinal region, disease status, or sex of subjects.

(A-E) RT-PCR data depicting fold change in *ISG15*, *OASL*, and *MX2* expression in small intestinal and colonic monolayers stimulated with IFNβ (100 or 300 IU/ml) or IFNλ2 (10 or 30 ng/ml) for 12 hrs according to intestinal region (A), disease status (B and C) or sex (D and E) of subjects. Each value is normalized to non-stimulated organoid lines. Data points are mean of at least 2 technical replicates of individual organoid lines. Bars represent mean ± SEM, and at least 2 independent experiments were performed. SI, small intestine. *$P \leq 0.05$ and **$P \leq 0.01$ by unpaired *t* test, two-tailed.

Supplemental figure 5. Stimulation with IFNβ or IFNλ2 does not alter *ACE2* and *TMPRSS2* expression in organoids.

(A and B) RT-PCR depicting *ACE2* (A) and *TMPRSS2* (B) expression in monolayers stimulated with IFNβ (100 or 300 IU/ml) or IFNλ2 (10 or 30 ng/ml) for 12 hrs. Data points are mean of at least 2 technical replicates of individual organoid lines. Bars represent mean ± SEM, and at least 2 independent experiments were performed. SI, small intestine.

Supplemental figure 6. Representative images of ACE2 staining in primary intestinal tissue.

(A and B) Representative ACE2 staining images in primary tissues of terminal ileum from which small intestinal (SI2-9 and 12, A) or colonic (C2-9, 11, and 12, B) organoid-derived monolayers were established. Images of remaining monolayers are included in main Figure 3. **(C)** Quantification of the total intensity of ACE2 staining and surface area in each visual field from the primary tissues from which the indicated organoid lines were established. Data points in C are the visual field. Bars in A and B: 200 μm. Bars in C represent mean ± SEM.

Supplemental figure 7. Transcriptome and viability of SARS-CoV-2-infected organoids.

(A) Viability according to MTT reduction assay of SARS-CoV-2-infected high infection (HI; C1, C2, and C3) and low infection (LI; C8, C12, and C13) lines. **(B and C)** RT-PCR data depicting *ACE2* (B) and *TMPRSS2* (C) expression in HI and LI monolayers with or without SARS-CoV-2 infection. **(D)** Number of up- and down-regulated genes identified by RNA-Seq analysis in the indicated pair-wise comparison of HI and LI monolayer lines at different time point post infection. n = 3 organoid lines per group and at least 2 technical replicates per individual organoid line. **(E)** Unsupervised clustering based on expression of most variable genes by organoids lines and infection with SARS-CoV-2 at 24 and 72 hrs. **(F)** Highly enriched molecular function GO terms for

the differentially expressed genes (DEGs) in HI and LI infected with SARS-CoV-2 for 72 hrs. **(G and H)** Heatmaps displaying normalized expression values of DEGs in HI infected/uninfected and LI infected/uninfected conditions (average fold-change ≥ 2 and adjusted *P*-value ≤ 0.05) annotated in GO:0060338 and GO:0034340 (G) and GO0:07259 (H) **(I)** Heatmap displaying normalized expression values of DEGs in LI infected/HI infected conditions (average fold-change ≥ 2 and adjusted *P*-value ≤ 0.05) annotated in GO:0006882. Data points in A-C are mean of at least 2 technical replicates of individual organoid lines. Bars represent mean ± SEM, and at least 2 independent experiments were performed. UI0, uninfected 0 hr; UI72, uninfected 72 hrs; I24, infected for 24 hrs; I72, infected for 72 hrs.

Supplemental figure 8. Transcript and Western blot analyses of BRG1, FOXM1, and FOXA2.
(A-C) RT-PCR analysis of *BRG1* (A), *FOXM1* (B), and *FOXA2* (C) expression in HI and LI monolayers. **(D)** Western blot analysis of BRG1, FOXM1, FOXA2, and ACTB in HI and LI monolayers. Blots are representative of at least 2 independent repeats. Data points are mean of at least 2 technical replicates of individual organoid lines. Bars represent mean ± SEM, and 2 independent experiments were performed. UI0, uninfected 0 hr; UI72, uninfected 72 hrs; I24, infected for 24 hrs; I72, infected for 72 hrs.

Supplemental figure 9. Infection of SARS-CoV-2 spike protein-pseudotyped lentiviral reporter viruses.
(A-B) HI and LI monolayers were infected with VSV-G or SARS-CoV-2 D614G, Delta, or Omciron spike protein pseudotyped viruses at an MOI of 0.2. At 72 hrs post-infection, infectivity was measured by luciferase assay. Data points are mean of at least 2 technical replicates of individual organoid lines. Bars represent mean ± SEM, and 2 independent experiments were performed. RLU, relative luminescence unit. ****$P \leq 0.0001$ by unpaired *t* test, two-tailed.

Table S1

Name	Tissue	Sex	Age	Disease type	Inflammation	ACE2 SNP
SI1	Terminal ileum	M	34	Non-IBD	Non-inflamed	NA
SI2	Terminal ileum	M	24	CD	Non-inflamed	NA
SI3	Terminal ileum	F	47	Non-IBD	Non-inflamed	ND
SI4	Terminal ileum	M	23	CD	Non-inflamed	ND
SI5	Terminal ileum	M	37	CD	Non-inflamed	NA
SI6	Terminal ileum	F	25	Non-IBD	Non-inflamed	NA
SI7	Terminal ileum	M	29	Non-IBD	Non-inflamed	ND
SI8	Terminal ileum	M	47	IBD	Non-inflamed	ND
SI9	Terminal ileum	F	37	CD	Non-inflamed	NA
SI10	Terminal ileum	F	69	CD	Non-inflamed	ND
SI11	Terminal ileum	F	23	Non-IBD	Non-inflamed	NA
SI12	Terminal ileum	M	39	CD	Non-inflamed	NA
C1	Ascending colon	M	34	Non-IBD	Non-inflamed	ND
C2	Ascending colon	M	25	Non-IBD	Non-inflamed	NA
C3	Ascending colon	F	55	UC	Non-inflamed	NA
C4	Ascending colon	F	27	UC	Non-inflamed	NA
C5	Ascending colon	M	29	Non-IBD	Non-inflamed	ND
C6	Ascending colon	M	33	UC	Non-inflamed	NA
C7	Ascending colon	M	33	UC	Non-inflamed	ND
C8	Ascending colon	F	23	Non-IBD	Non-inflamed	ND
C9	Ascending colon	M	24	CD	Non-inflamed	NA
C10	Ascending colon	M	37	CD	Non-inflamed	NA
C11	Ascending colon	F	37	CD	Non-inflamed	NA
C12	Ascending colon	M	21	UC	Non-inflamed	NA
C13	Ascending colon	F	20	UC	Non-inflamed	ND

Supplemental Table 1. Subject information for human endoscopic specimens

M; Male, F; Female, CD; Crohn's disease; UC; Ulcerative colitis; SNP, Single nucleotide polymorphism; ND, not detected; NA, not attempted

690 **Table S2**

Gene expression	Age					
	SI + Colon		SI		Colon	
	r	*P*	r	*P*	r	*P*
ACE2	-0.056	0.790	-0.329	0.296	0.323	0.282
TMPRSS2	-0.122	0.562	-0.144	0.656	0.068	0.826
TMPRSS4	-0.018	0.931	0.158	0.626	0.320	0.287
APOA1	0.187	0.371	0.041	0.900	-0.235	0.439
ISG15	-0.203	0.330	-0.243	0.446	-0.145	0.636
OASL	0.004	0.985	-0.196	0.541	0.263	0.386
MX2	0.077	0.717	0.157	0.626	-0.018	0.953

691

692 **Supplemental Table 2**. Correlation between subject age and gene expression among the
693 organoid monolayers grown in differentiation media for 7 days. *r*, Pearson correlation coefficient;
694 *P*, *P*-value; SI, small intestine.

695

Table S3

Gene induction	Age				SARS-CoV-2 replication			
	SI		Colon		SI		Colon	
	r	*P*	*r*	*P*	*r*	*P*	*r*	*P*
ISG15								
100 IU/ml IFNβ	0.384	0.218	0.076	0.806	0.109	0.736	0.146	0.633
300 IU/ml IFNβ	0.311	0.326	0.041	0.894	-0.079	0.806	-0.148	0.630
10 ng/ml IFNλ2	0.433	0.160	-0.206	0.499	-0.071	0.827	-0.131	0.671
30 ng/ml IFNλ2	0.457	0.135	-0.082	0.791	-0.393	0.206	-0.028	0.927
OASL								
100 IU/ml IFNβ	0.835	*0.001***	-0.344	0.250	-0.424	0.169	-0.033	0.916
300 IU/ml IFNβ	0.668	*0.018**	0.103	0.738	-0.300	0.344	-0.096	0.755
10 ng/ml IFNλ2	0.538	0.071	-0.173	0.572	-0.404	0.193	-0.110	-0.720
30 ng/ml IFNλ2	0.623	0.030*	0.430	0.143	-0.274	0.390	-0.163	0.596
MX2								
100 IU/ml IFNβ	-0.250	0.432	-0.102	0.741	0.308	0.331	0.006	0.985
300 IU/ml IFNβ	-0.128	0.691	-0.057	0.853	0.250	0.433	0.015	0.689
10 ng/ml IFNλ2	-0.311	0.326	-0.150	0.626	0.091	0.779	-0.194	0.526
30 ng/ml IFNλ2	0.239	0.454	-0.091	0.768	0.171	0.595	0.013	0.966

Supplemental Table 3. Correlation of subject age or PFU of SARS-CoV-2 with ISG induction in organoids stimulated with IFNβ (100 or 300 IU/ml) or IFNλ2 (10 or 30 ng/ml) for 12 hrs. *r*, Pearson correlation coefficient; *P*, *P*-value; SI, small intestine. *$P \leq 0.05$ and ***$P \leq 0.001$ by simple regression analysis.

References

1. Fujii M, Sato T. Somatic cell-derived organoids as prototypes of human epithelial tissues and diseases. Nat Mater. 2020.
2. Geiser P, Di Martino ML, Samperio Ventayol P, Eriksson J, Sima E, Al-Saffar AK, et al. Salmonella enterica Serovar Typhimurium Exploits Cycling through Epithelial Cells To Colonize Human and Murine Enteroids. mBio. 2021;12(1).
3. Finkbeiner SR, Zeng XL, Utama B, Atmar RL, Shroyer NF, Estes MK. Stem cell-derived human intestinal organoids as an infection model for rotaviruses. mBio. 2012;3(4):e00159-12.
4. Hosmillo M, Chaudhry Y, Nayak K, Sorgeloos F, Koo BK, Merenda A, et al. Norovirus Replication in Human Intestinal Epithelial Cells Is Restricted by the Interferon-Induced JAK/STAT Signaling Pathway and RNA Polymerase II-Mediated Transcriptional Responses. mBio. 2020;11(2).
5. Drost J, Clevers H. Organoids in cancer research. Nat Rev Cancer. 2018;18(7):407-18.
6. Nanki K, Fujii M, Shimokawa M, Matano M, Nishikori S, Date S, et al. Somatic inflammatory gene mutations in human ulcerative colitis epithelium. Nature. 2020;577(7789):254-9.
7. Matsuzawa-Ishimoto Y, Hine A, Shono Y, Rudensky E, Lazrak A, Yeung F, et al. An intestinal organoid-based platform that recreates susceptibility to T-cell-mediated tissue injury. Blood. 2020;135(26):2388-401.
8. Borten MA, Bajikar SS, Sasaki N, Clevers H, Janes KA. Automated brightfield morphometry of 3D organoid populations by OrganoSeg. Sci Rep. 2018;8(1):5319.
9. Luo X, Zhou GZ, Zhang Y, Peng LH, Zou LP, Yang YS. Coronaviruses and gastrointestinal diseases. Mil Med Res. 2020;7(1):49.
10. Ye L, Yang Z, Liu J, Liao L, Wang F. Digestive system manifestations and clinical significance of coronavirus disease 2019: A systematic literature review. J Gastroenterol Hepatol. 2020.
11. D'Amico F, Baumgart DC, Danese S, Peyrin-Biroulet L. Diarrhea During COVID-19 Infection: Pathogenesis, Epidemiology, Prevention, and Management. Clin Gastroenterol Hepatol. 2020;18(8):1663-72.
12. Gupta A, Madhavan MV, Sehgal K, Nair N, Mahajan S, Sehrawat TS, et al. Extrapulmonary manifestations of COVID-19. Nat Med. 2020;26(7):1017-32.
13. Redd WD, Zhou JC, Hathorn KE, McCarty TR, Bazarbashi AN, Thompson CC, et al. Prevalence and Characteristics of Gastrointestinal Symptoms in Patients With Severe Acute Respiratory Syndrome Coronavirus 2 Infection in the United States: A Multicenter Cohort Study. Gastroenterology. 2020;159(2):765-7 e2.
14. Cheung KS, Hung IFN, Chan PPY, Lung KC, Tso E, Liu R, et al. Gastrointestinal Manifestations of SARS-CoV-2 Infection and Virus Load in Fecal Samples From a Hong Kong Cohort: Systematic Review and Meta-analysis. Gastroenterology. 2020;159(1):81-95.
15. Nobel YR, Phipps M, Zucker J, Lebwohl B, Wang TC, Sobieszczyk ME, et al. Gastrointestinal Symptoms and Coronavirus Disease 2019: A Case-Control Study From the United States. Gastroenterology. 2020;159(1):373-5 e2.
16. Aghemo A, Piovani D, Parigi TL, Brunetta E, Pugliese N, Vespa E, et al. COVID-19 Digestive System Involvement and Clinical Outcomes in a Large Academic Hospital in Milan, Italy. Clin Gastroenterol Hepatol. 2020;18(10):2366-8 e3.

17. Gaebler C, Wang Z, Lorenzi JCC, Muecksch F, Finkin S, Tokuyama M, et al. Evolution of antibody immunity to SARS-CoV-2. Nature. 2021;591(7851):639-44.
18. Morone G, Palomba A, Iosa M, Caporaso T, De Angelis D, Venturiero V, et al. Incidence and Persistence of Viral Shedding in COVID-19 Post-acute Patients With Negativized Pharyngeal Swab: A Systematic Review. Front Med (Lausanne). 2020;7:562.
19. Park SK, Lee CW, Park DI, Woo HY, Cheong HS, Shin HC, et al. Detection of SARS-CoV-2 in Fecal Samples From Patients With Asymptomatic and Mild COVID-19 in Korea. Clin Gastroenterol Hepatol. 2020.
20. Wolfel R, Corman VM, Guggemos W, Seilmaier M, Zange S, Muller MA, et al. Virological assessment of hospitalized patients with COVID-2019. Nature. 2020;581(7809):465-9.
21. Holshue ML, DeBolt C, Lindquist S, Lofy KH, Wiesman J, Bruce H, et al. First Case of 2019 Novel Coronavirus in the United States. N Engl J Med. 2020;382(10):929-36.
22. Guan WJ, Ni ZY, Hu Y, Liang WH, Ou CQ, He JX, et al. Clinical Characteristics of Coronavirus Disease 2019 in China. N Engl J Med. 2020;382(18):1708-20.
23. Xiao F, Tang M, Zheng X, Liu Y, Li X, Shan H. Evidence for Gastrointestinal Infection of SARS-CoV-2. Gastroenterology. 2020;158(6):1831-3 e3.
24. Coryell MP, Iakiviak M, Pereira N, Murugkar PP, Rippe J, Williams DB, et al. A method for detection of SARS-CoV-2 RNA in healthy human stool: a validation study. Lancet Microbe. 2021.
25. Livanos AE, Jha D, Cossarini F, Gonzalez-Reiche AS, Tokuyama M, Aydillo T, et al. Gastrointestinal involvement attenuates COVID-19 severity and mortality. medRxiv. 2020.
26. Effenberger M, Grabherr F, Mayr L, Schwaerzler J, Nairz M, Seifert M, et al. Faecal calprotectin indicates intestinal inflammation in COVID-19. Gut. 2020;69(8):1543-4.
27. Britton GJ, Chen-Liaw A, Cossarini F, Livanos AE, Spindler MP, Plitt T, et al. SARS-CoV-2-specific IgA and limited inflammatory cytokines are present in the stool of select patients with acute COVID-19. medRxiv. 2020.
28. Xiao F, Sun J, Xu Y, Li F, Huang X, Li H, et al. Infectious SARS-CoV-2 in Feces of Patient with Severe COVID-19. Emerg Infect Dis. 2020;26(8):1920-2.
29. Bradley BT, Maioli H, Johnston R, Chaudhry I, Fink SL, Xu H, et al. Histopathology and ultrastructural findings of fatal COVID-19 infections in Washington State: a case series. Lancet. 2020;396(10247):320-32.
30. Ziegler CGK, Allon SJ, Nyquist SK, Mbano IM, Miao VN, Tzouanas CN, et al. SARS-CoV-2 Receptor ACE2 Is an Interferon-Stimulated Gene in Human Airway Epithelial Cells and Is Detected in Specific Cell Subsets across Tissues. Cell. 2020;181(5):1016-35 e19.
31. Muus C, Luecken MD, Eraslan G, Sikkema L, Waghray A, Heimberg G, et al. Single-cell meta-analysis of SARS-CoV-2 entry genes across tissues and demographics. Nat Med. 2021;27(3):546-59.
32. Zang R, Gomez Castro MF, McCune BT, Zeng Q, Rothlauf PW, Sonnek NM, et al. TMPRSS2 and TMPRSS4 promote SARS-CoV-2 infection of human small intestinal enterocytes. Sci Immunol. 2020;5(47).
33. Lamers MM, Beumer J, van der Vaart J, Knoops K, Puschhof J, Breugem TI, et al. SARS-CoV-2 productively infects human gut enterocytes. Science. 2020;369(6499):50-4.
34. Zhou J, Li C, Liu X, Chiu MC, Zhao X, Wang D, et al. Infection of bat and human intestinal organoids by SARS-CoV-2. Nat Med. 2020;26(7):1077-83.

795 35. Stanifer ML, Kee C, Cortese M, Zumaran CM, Triana S, Mukenhirn M, et al. Critical
796 Role of Type III Interferon in Controlling SARS-CoV-2 Infection in Human Intestinal Epithelial
797 Cells. Cell Rep. 2020;32(1):107863.
798 36. Vuille-Dit-Bille RN, Liechty KW, Verrey F, Guglielmetti LC. SARS-CoV-2 receptor
799 ACE2 gene expression in small intestine correlates with age. Amino Acids. 2020;52(6-7):1063-
800 5.
801 37. Penninger JM, Grant MB, Sung JJY. The Role of Angiotensin Converting Enzyme 2 in
802 Modulating Gut Microbiota, Intestinal Inflammation, and Coronavirus Infection.
803 Gastroenterology. 2021;160(1):39-46.
804 38. Potdar AA, Dube S, Naito T, Li K, Botwin G, Haritunians T, et al. Altered Intestinal
805 ACE2 Levels Are Associated With Inflammation, Severe Disease, and Response to Anti-
806 Cytokine Therapy in Inflammatory Bowel Disease. Gastroenterology. 2021;160(3):809-22 e7.
807 39. Suarez-Farinas M, Tokuyama M, Wei G, Huang R, Livanos A, Jha D, et al. Intestinal
808 Inflammation Modulates the Expression of ACE2 and TMPRSS2 and Potentially Overlaps With
809 the Pathogenesis of SARS-CoV-2-related Disease. Gastroenterology. 2021;160(1):287-301 e20.
810 40. Triana S, Metz-Zumaran C, Ramirez C, Kee C, Doldan P, Shahraz M, et al. Single-cell
811 analyses reveal SARS-CoV-2 interference with intrinsic immune response in the human gut. Mol
812 Syst Biol. 2021;17(4):e10232.
813 41. Zhang H, Li HB, Lyu JR, Lei XM, Li W, Wu G, et al. Specific ACE2 expression in
814 small intestinal enterocytes may cause gastrointestinal symptoms and injury after 2019-nCoV
815 infection. Int J Infect Dis. 2020;96:19-24.
816 42. Potdar AA, Dube S, Naito T, Botwin G, Haritunians T, Li D, et al. Reduced expression
817 of COVID-19 host receptor, ACE2 is associated with small bowel inflammation, more severe
818 disease, and response to anti-TNF therapy in Crohn's disease. medRxiv. 2020.
819 43. Lanjanian H, Moazzam-Jazi M, Hedayati M, Akbarzadeh M, Guity K, Sedaghati-Khayat
820 B, et al. SARS-CoV-2 infection susceptibility influenced by ACE2 genetic polymorphisms:
821 insights from Tehran Cardio-Metabolic Genetic Study. Sci Rep. 2021;11(1):1529.
822 44. Guo X, Chen Z, Xia Y, Lin W, Li H. Investigation of the genetic variation in ACE2 on
823 the structural recognition by the novel coronavirus (SARS-CoV-2). J Transl Med.
824 2020;18(1):321.
825 45. Calcagnile M, Forgez P, Iannelli A, Bucci C, Alifano M, Alifano P. Molecular docking
826 simulation reveals ACE2 polymorphisms that may increase the affinity of ACE2 with the SARS-
827 CoV-2 Spike protein. Biochimie. 2021;180:143-8.
828 46. Khayat AS, de Assumpcao PP, Meireles Khayat BC, Thomaz Araujo TM, Batista-
829 Gomes JA, Imbiriba LC, et al. ACE2 polymorphisms as potential players in COVID-19
830 outcome. PLoS One. 2020;15(12):e0243887.
831 47. Busnadiego I, Fernbach S, Pohl MO, Karakus U, Huber M, Trkola A, et al. Antiviral
832 Activity of Type I, II, and III Interferons Counterbalances ACE2 Inducibility and Restricts
833 SARS-CoV-2. mBio. 2020;11(5).
834 48. Cheemarla NR, Watkins TA, Mihaylova VT, Wang B, Zhao D, Wang G, et al.
835 Magnitude and timing of the antiviral response determine SARS-CoV-2 replication early in
836 infection. medRxiv. 2021.
837 49. Lowery SA, Sariol A, Perlman S. Innate immune and inflammatory responses to SARS-
838 CoV-2: Implications for COVID-19. Cell Host Microbe. 2021.

50. Sato T, Stange DE, Ferrante M, Vries RG, Van Es JH, Van den Brink S, et al. Long-term expansion of epithelial organoids from human colon, adenoma, adenocarcinoma, and Barrett's epithelium. Gastroenterology. 2011;141(5):1762-72.
51. Middendorp S, Schneeberger K, Wiegerinck CL, Mokry M, Akkerman RD, van Wijngaarden S, et al. Adult stem cells in the small intestine are intrinsically programmed with their location-specific function. Stem Cells. 2014;32(5):1083-91.
52. Lei X, Dong X, Ma R, Wang W, Xiao X, Tian Z, et al. Activation and evasion of type I interferon responses by SARS-CoV-2. Nat Commun. 2020;11(1):3810.
53. Chen X, Saccon E, Appelberg KS, Mikaeloff F, Rodriguez JE, Vinhas BS, et al. Type-I interferon signatures in SARS-CoV-2 infected Huh7 cells. Cell Death Discov. 2021;7(1):114.
54. Ghoshal K, Majumder S, Zhu Q, Hunzeker J, Datta J, Shah M, et al. Influenza virus infection induces metallothionein gene expression in the mouse liver and lung by overlapping but distinct molecular mechanisms. Mol Cell Biol. 2001;21(24):8301-17.
55. Ilback NG, Glynn AW, Wikberg L, Netzel E, Lindh U. Metallothionein is induced and trace element balance changed in target organs of a common viral infection. Toxicology. 2004;199(2-3):241-50.
56. Pedersen KB, Chodavarapu H, Lazartigues E. Forkhead Box Transcription Factors of the FOXA Class Are Required for Basal Transcription of Angiotensin-Converting Enzyme 2. J Endocr Soc. 2017;1(4):370-84.
57. Yang J, Feng X, Zhou Q, Cheng W, Shang C, Han P, et al. Pathological Ace2-to-Ace enzyme switch in the stressed heart is transcriptionally controlled by the endothelial Brg1-FoxM1 complex. Proc Natl Acad Sci U S A. 2016;113(38):E5628-35.
58. Tada T, Fan C, Chen JS, Kaur R, Stapleford KA, Gristick H, et al. An ACE2 Microbody Containing a Single Immunoglobulin Fc Domain Is a Potent Inhibitor of SARS-CoV-2. Cell Rep. 2020;33(12):108528.
59. Wu L, Zhou L, Mo M, Liu T, Wu C, Gong C, et al. SARS-CoV-2 Omicron RBD shows weaker binding affinity than the currently dominant Delta variant to human ACE2. Signal Transduct Target Ther. 2022;7(1):8.
60. Mannar D, Saville JW, Zhu X, Srivastava SS, Berezuk AM, Tuttle KS, et al. SARS-CoV-2 Omicron Variant: ACE2 Binding, Cryo-EM Structure of Spike Protein-ACE2 Complex and Antibody Evasion. bioRxiv. 2021:2021.12.19.473380.
61. Peacock TP, Brown JC, Zhou J, Thakur N, Newman J, Kugathasan R, et al. The SARS-CoV-2 variant, Omicron, shows rapid replication in human primary nasal epithelial cultures and efficiently uses the endosomal route of entry. bioRxiv. 2022:2021.12.31.474653.
62. Carrera G, Paternain JL, Carrere N, Folch J, Courtade-Saidi M, Orfila C, et al. Hepatic metallothionein in patients with chronic hepatitis C: relationship with severity of liver disease and response to treatment. Am J Gastroenterol. 2003;98(5):1142-9.
63. Read SA, Parnell G, Booth D, Douglas MW, George J, Ahlenstiel G. The antiviral role of zinc and metallothioneins in hepatitis C infection. J Viral Hepat. 2018;25(5):491-501.
64. Panchariya L, Khan WA, Kuila S, Sonkar K, Sahoo S, Ghoshal A, et al. Zinc(2+) ion inhibits SARS-CoV-2 main protease and viral replication in vitro. Chem Commun (Camb). 2021;57(78):10083-6.
65. Kanekiyo M, Itoh N, Kawasaki A, Tanaka J, Nakanishi T, Tanaka K. Zinc-induced activation of the human cytomegalovirus major immediate-early promoter is mediated by metallothionein and nuclear factor-kappaB. Toxicol Appl Pharmacol. 2001;173(3):146-53.

884 66. Abt MC, Buffie CG, Susac B, Becattini S, Carter RA, Leiner I, et al. TLR-7 activation
885 enhances IL-22-mediated colonization resistance against vancomycin-resistant enterococcus. Sci
886 Transl Med. 2016;8(327):327ra25.
887 67. Kernbauer E, Ding Y, Cadwell K. An enteric virus can replace the beneficial function of
888 commensal bacteria. Nature. 2014;516(7529):94-8.
889 68. Neil JA, Matsuzawa-Ishimoto Y, Kernbauer-Holzl E, Schuster SL, Sota S, Venzon M, et
890 al. IFN-I and IL-22 mediate protective effects of intestinal viral infection. Nat Microbiol.
891 2019;4(10):1737-49.
892 69. Van Winkle JA, Constant DA, Li L, Nice TJ. Selective Interferon Responses of
893 Intestinal Epithelial Cells Minimize Tumor Necrosis Factor Alpha Cytotoxicity. J Virol.
894 2020;94(21).
895 70. Sun L, Miyoshi H, Origanti S, Nice TJ, Barger AC, Manieri NA, et al. Type I
896 Interferons Link Viral Infection to Enhanced Epithelial Turnover and Repair. Cell Host Microbe.
897 2014.
898 71. Aden K, Tran F, Ito G, Sheibani-Tezerji R, Lipinski S, Kuiper JW, et al. ATG16L1
899 orchestrates interleukin-22 signaling in the intestinal epithelium via cGAS-STING. J Exp Med.
900 2018;215(11):2868-86.
901 72. Liu L, Gong T, Tao W, Lin B, Li C, Zheng X, et al. Commensal viruses maintain
902 intestinal intraepithelial lymphocytes via noncanonical RIG-I signaling. Nat Immunol.
903 2019;20(12):1681-91.
904 73. Broggi A, Tan Y, Granucci F, Zanoni I. IFN-lambda suppresses intestinal inflammation
905 by non-translational regulation of neutrophil function. Nat Immunol. 2017;18(10):1084-93.
906 74. Yang JY, Kim MS, Kim E, Cheon JH, Lee YS, Kim Y, et al. Enteric Viruses Ameliorate
907 Gut Inflammation via Toll-like Receptor 3 and Toll-like Receptor 7-Mediated Interferon-beta
908 Production. Immunity. 2016;44(4):889-900.
909 75. Martin PK, Marchiando A, Xu R, Rudensky E, Yeung F, Schuster SL, et al. Autophagy
910 proteins suppress protective type I interferon signalling in response to the murine gut microbiota.
911 Nat Microbiol. 2018;3(10):1131-41.
912 76. Matsuzawa-Ishimoto Y, Shono Y, Gomez LE, Hubbard-Lucey VM, Cammer M, Neil J,
913 et al. Autophagy protein ATG16L1 prevents necroptosis in the intestinal epithelium. J Exp Med.
914 2017;214(12):3687-705.
915 77. Wu Y, Cheng X, Jiang G, Tang H, Ming S, Tang L, et al. Altered oral and gut
916 microbiota and its association with SARS-CoV-2 viral load in COVID-19 patients during
917 hospitalization. NPJ Biofilms Microbiomes. 2021;7(1):61.
918 78. Yeoh YK, Zuo T, Lui GC, Zhang F, Liu Q, Li AY, et al. Gut microbiota composition
919 reflects disease severity and dysfunctional immune responses in patients with COVID-19. Gut.
920 2021;70(4):698-706.
921 79. Zhang F, Wan Y, Zuo T, Yeoh YK, Liu Q, Zhang L, et al. Prolonged Impairment of
922 Short-Chain Fatty Acid and L-Isoleucine Biosynthesis in Gut Microbiome in Patients With
923 COVID-19. Gastroenterology. 2021.
924 80. Venzon M, Bernard L, Klein J, Axelrad JE, Hussey GA, Sullivan AP, et al. Gut
925 microbiome dysbiosis during COVID-19 is associated with increased risk for bacteremia and
926 microbial translocation. bioRxiv. 2021:2021.07.15.452246.
927 81. Vandesompele J, De Preter K, Pattyn F, Poppe B, Van Roy N, De Paepe A, et al.
928 Accurate normalization of real-time quantitative RT-PCR data by geometric averaging of
929 multiple internal control genes. Genome Biol. 2002;3(7):RESEARCH0034.

930 82. Li W, Moore MJ, Vasilieva N, Sui J, Wong SK, Berne MA, et al. Angiotensin-
931 converting enzyme 2 is a functional receptor for the SARS coronavirus. Nature.
932 2003;426(6965):450-4.
933 83. Xie X, Muruato A, Lokugamage KG, Narayanan K, Zhang X, Zou J, et al. An Infectious
934 cDNA Clone of SARS-CoV-2. Cell Host Microbe. 2020;27(5):841-8 e3.
935 84. Lee IT, Nakayama T, Wu CT, Goltsev Y, Jiang S, Gall PA, et al. ACE2 localizes to the
936 respiratory cilia and is not increased by ACE inhibitors or ARBs. Nat Commun.
937 2020;11(1):5453.
938 85. Tada T, Zhou H, Dcosta BM, Samanovic MI, Chivukula V, Herati RS, et al. Increased
939 resistance of SARS-CoV-2 Omicron Variant to Neutralization by Vaccine-Elicited and
940 Therapeutic Antibodies. bioRxiv. 2021:2021.12.28.474369.
941

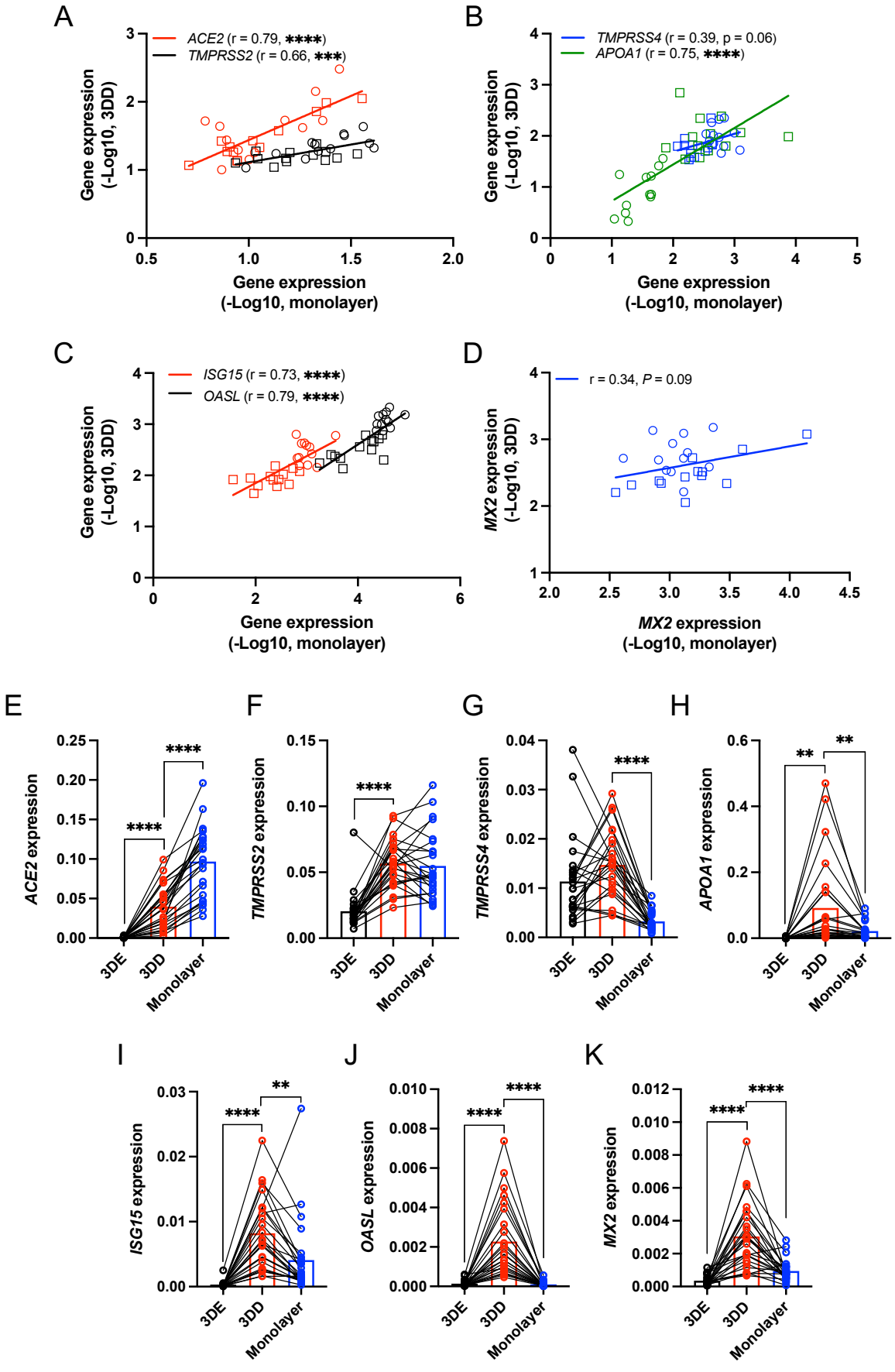
A
ACE2 (r = 0.79, ****)
TMPRSS2 (r = 0.66, ***)
Gene expression (-Log10, 3DD)
Gene expression (-Log10, monolayer)
B
TMPRSS4 (r = 0.39, p = 0.06)
APOA1 (r = 0.75, ****)
Gene expression (-Log10, 3DD)
Gene expression (-Log10, monolayer)
C
ISG15 (r = 0.73, ****)
OASL (r = 0.79, ****)
Gene expression (-Log10, 3DD)
Gene expression (-Log10, monolayer)
D
r = 0.34, P = 0.09
MX2 expression (-Log10, 3DD)
MX2 expression (-Log10, monolayer)
E
ACE2 expression
F
TMPRSS2 expression
G
TMPRSS4 expression
H
APOA1 expression
I
ISG15 expression
J
OASL expression
K
MX2 expression
3DE
3DD
Monolayer

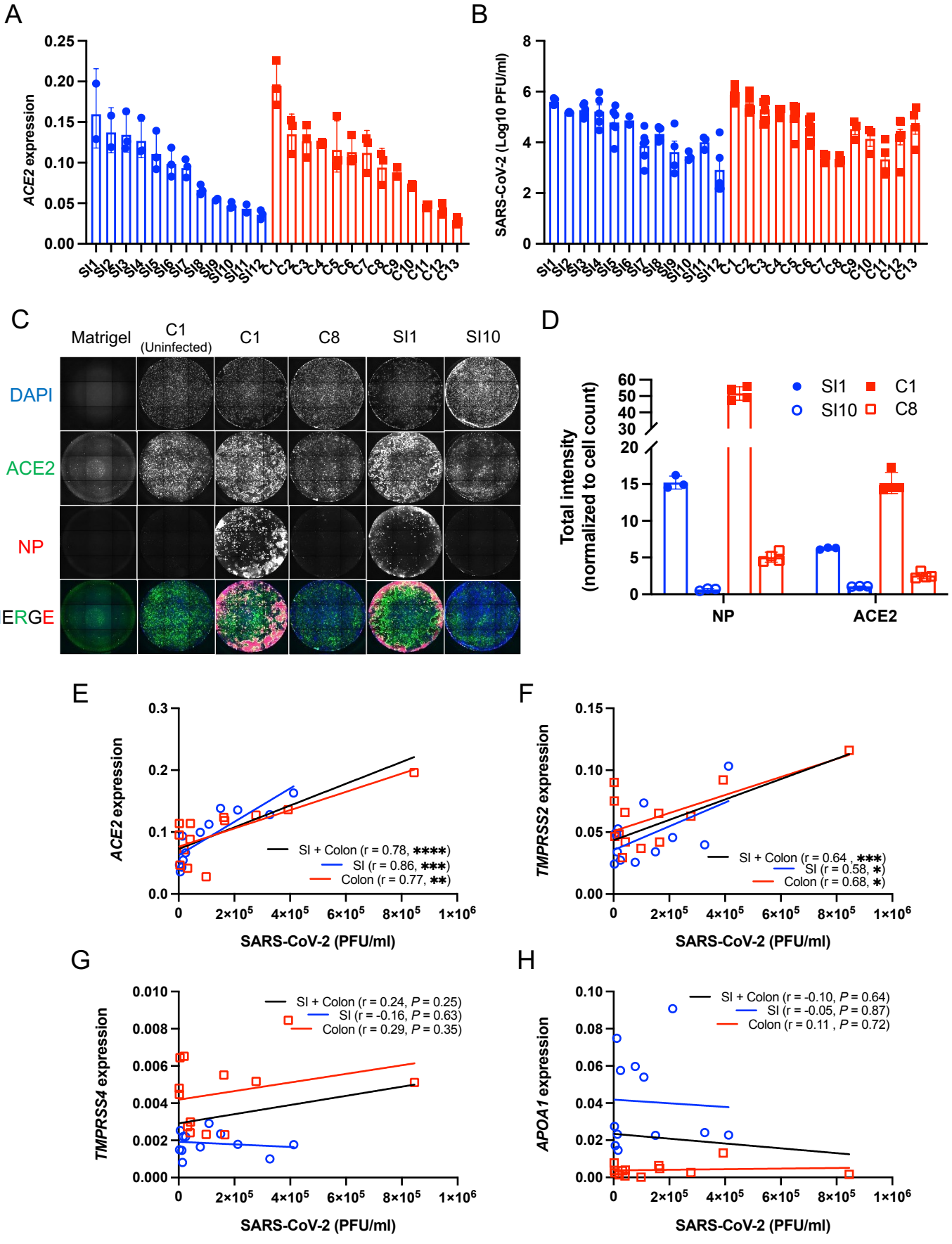
A
ACE2 expression
0.25
0.20
0.15
0.10
0.05
0.00
SI1 SI2 SI3 SI4 SI5 SI6 SI7 SI8 SI9 SI10 SI11 SI12 C1 C2 C3 C4 C5 C6 C7 C8 C9 C10 C11 C12 C13
B
SARS-CoV-2 (Log10 PFU/ml)
8
6
4
2
0
SI1 SI2 SI3 SI4 SI5 SI6 SI7 SI8 SI9 SI10 SI11 SI12 C1 C2 C3 C4 C5 C6 C7 C8 C9 C10 C11 C12 C13
C
Matrigel
C1 (Uninfected)
C1
C8
SI1
SI10
DAPI
ACE2
NP
MERGE
D
Total intensity (normalized to cell count)
60
50
40
30
20
15
10
5
0
SI1
SI10
C1
C8
NP
ACE2
E
ACE2 expression
0.3
0.2
0.1
0.0
SI + Colon (r = 0.78, ****)
SI (r = 0.86, ***)
Colon (r = 0.77, **)
0
2×10^5
4×10^5
6×10^5
8×10^5
1×10^6
SARS-CoV-2 (PFU/ml)
F
TMPRSS2 expression
0.15
0.10
0.05
0.00
SI + Colon (r = 0.64 , ***)
SI (r = 0.58, *)
Colon (r = 0.68, *)
SARS-CoV-2 (PFU/ml)
G
TMPRSS4 expression
0.010
0.008
0.006
0.004
0.002
0.000
SI + Colon (r = 0.24, P = 0.25)
SI (r = -0.16, P = 0.63)
Colon (r = 0.29, P = 0.35)
SARS-CoV-2 (PFU/ml)
H
APOA1 expression
0.10
0.08
0.06
0.04
0.02
0.00
SI + Colon (r = -0.10, P = 0.64)
SI (r = -0.05, P = 0.87)
Colon (r = 0.11 , P = 0.72)
SARS-CoV-2 (PFU/ml)

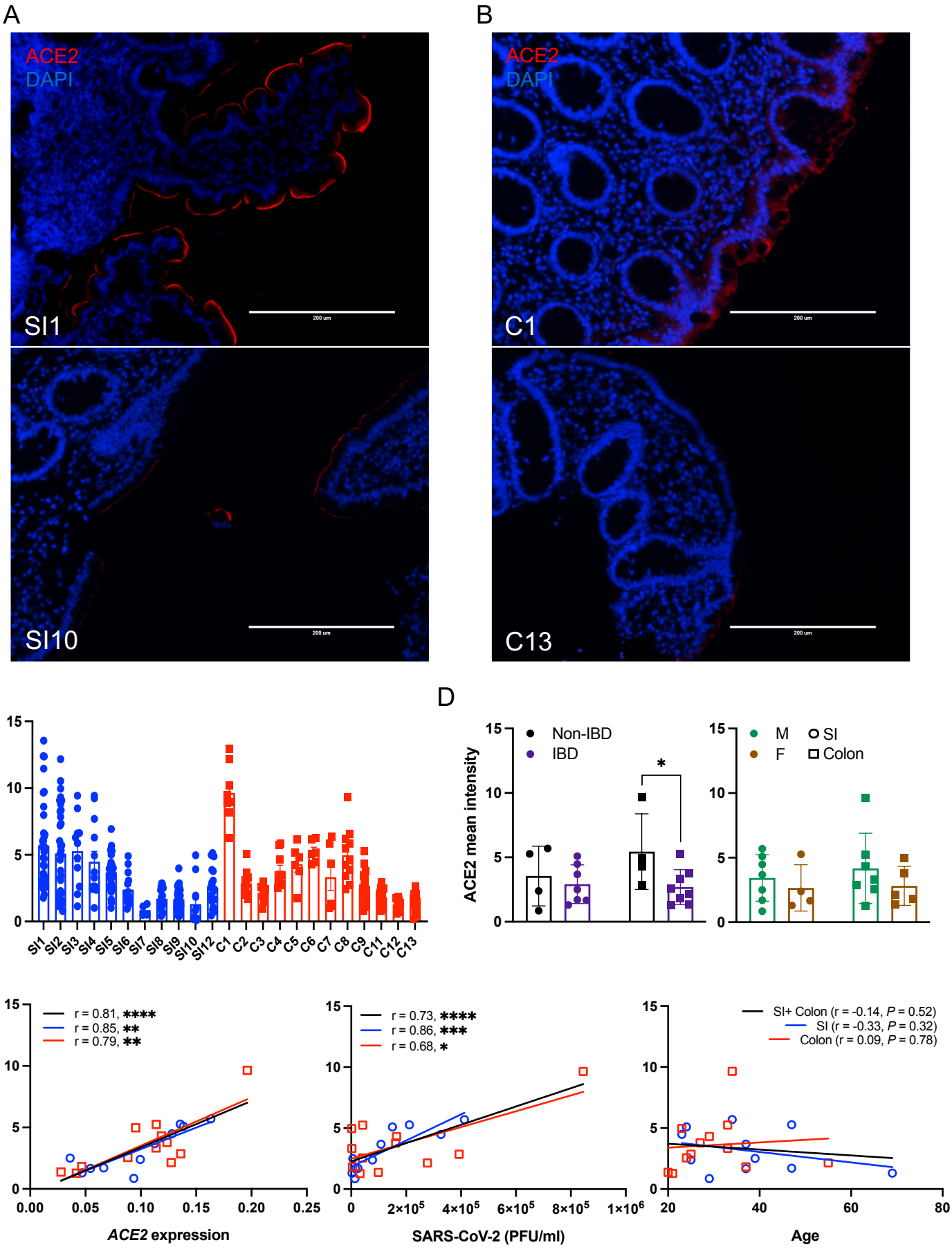
A
ACE2
DAPI
SI1
200 um
SI10
200 um
B
ACE2
DAPI
C1
200 um
C13
200 um
C
ACE2 mean intensity
0
5
10
15
SI1 SI2 SI3 SI4 SI5 SI6 SI7 SI8 SI9 SI10 SI12 C1 C2 C3 C4 C5 C6 C7 C8 C9 C11 C12 C13
D
ACE2 mean intensity
Non-IBD
IBD
*
M
F
SI
Colon
E
ACE2 mean intensity
r = 0.81, ****
r = 0.85, **
r = 0.79, **
ACE2 expression
r = 0.73, ****
r = 0.86, ***
r = 0.68, *
SARS-CoV-2 (PFU/ml)
SI+ Colon (r = -0.14, P = 0.52)
SI (r = -0.33, P = 0.32)
Colon (r = 0.09, P = 0.78)
Age

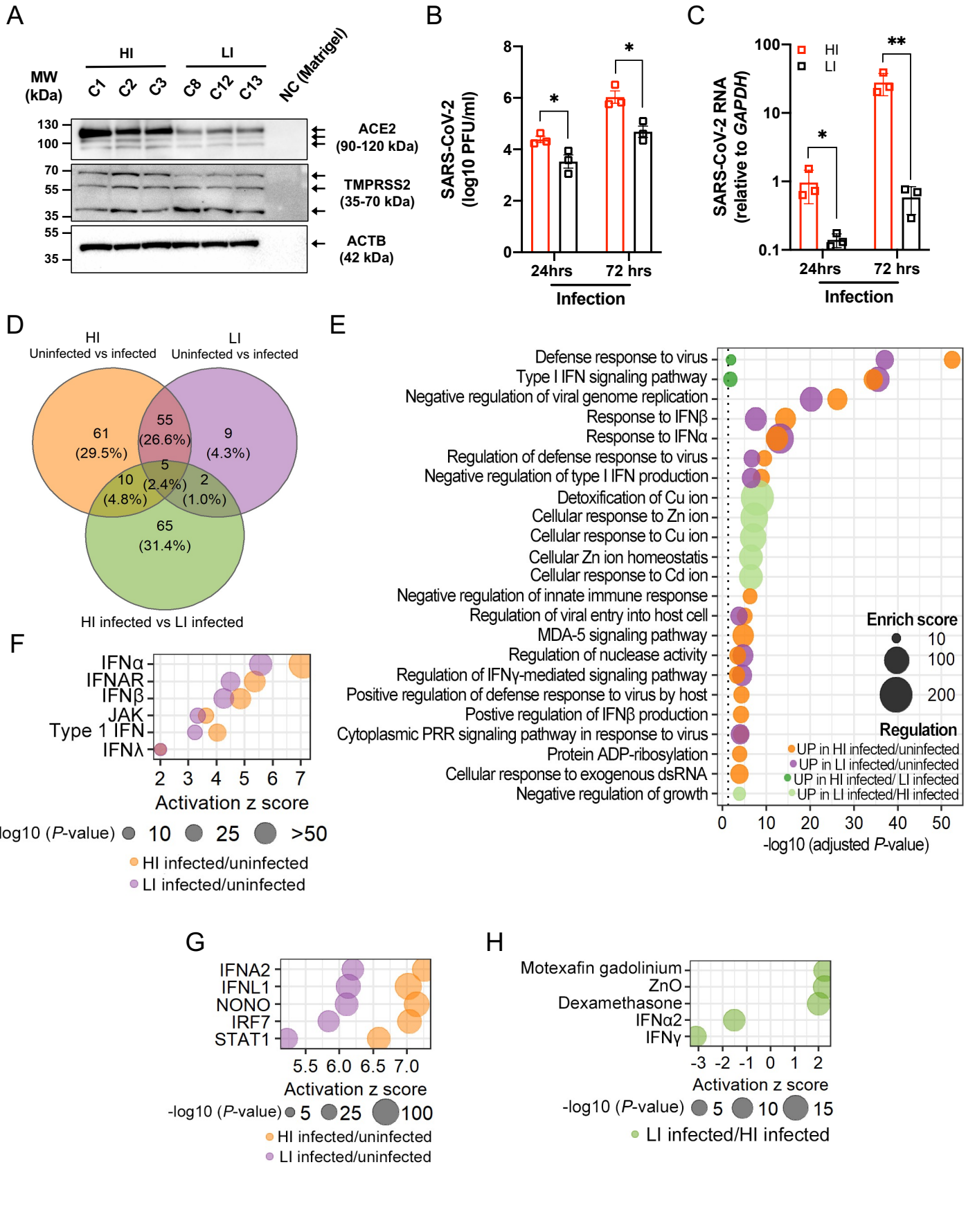
A
HI
LI
MW (kDa)
C-1
C-2
C-3
C-8
C-12
C-13
NC (Matrigel)
130
100
70
55
35
55
35
ACE2 (90-120 kDa)
TMPRSS2 (35-70 kDa)
ACTB (42 kDa)
B
SARS-CoV-2 (log10 PFU/ml)
24hrs
72 hrs
Infection
C
SARS-CoV-2 RNA (relative to GAPDH)
HI
LI
24hrs
72 hrs
Infection
D
HI
Uninfected vs infected
LI
Uninfected vs infected
61 (29.5%)
55 (26.6%)
9 (4.3%)
5 (2.4%)
10 (4.8%)
2 (1.0%)
65 (31.4%)
HI infected vs LI infected
E
Defense response to virus
Type I IFN signaling pathway
Negative regulation of viral genome replication
Response to IFNβ
Response to IFNα
Regulation of defense response to virus
Negative regulation of type I IFN production
Detoxification of Cu ion
Cellular response to Zn ion
Cellular response to Cu ion
Cellular Zn ion homeostatis
Cellular response to Cd ion
Negative regulation of innate immune response
Regulation of viral entry into host cell
MDA-5 signaling pathway
Regulation of nuclease activity
Regulation of IFNγ-mediated signaling pathway
Positive regulation of defense response to virus by host
Postive regulation of IFNβ production
Cytoplasmic PRR signaling pathway in response to virus
Protein ADP-ribosylation
Cellular response to exogenous dsRNA
Negative regulation of growth
Enrich score
10
100
200
Regulation
UP in HI infected/uninfected
UP in LI infected/uninfected
UP in HI infected/ LI infected
UP in LI infected/HI infected
-log10 (adjusted P-value)
F
IFNα
IFNAR
IFNβ
JAK
Type 1 IFN
IFNλ
Activation z score
-log10 (P-value) 10 25 >50
HI infected/uninfected
LI infected/uninfected
G
IFNA2
IFNL1
NONO
IRF7
STAT1
Activation z score
-log10 (P-value) 5 25 100
HI infected/uninfected
LI infected/uninfected
H
Motexafin gadolinium
ZnO
Dexamethasone
IFNα2
IFNγ
Activation z score
-log10 (P-value) 5 10 15
LI infected/HI infected

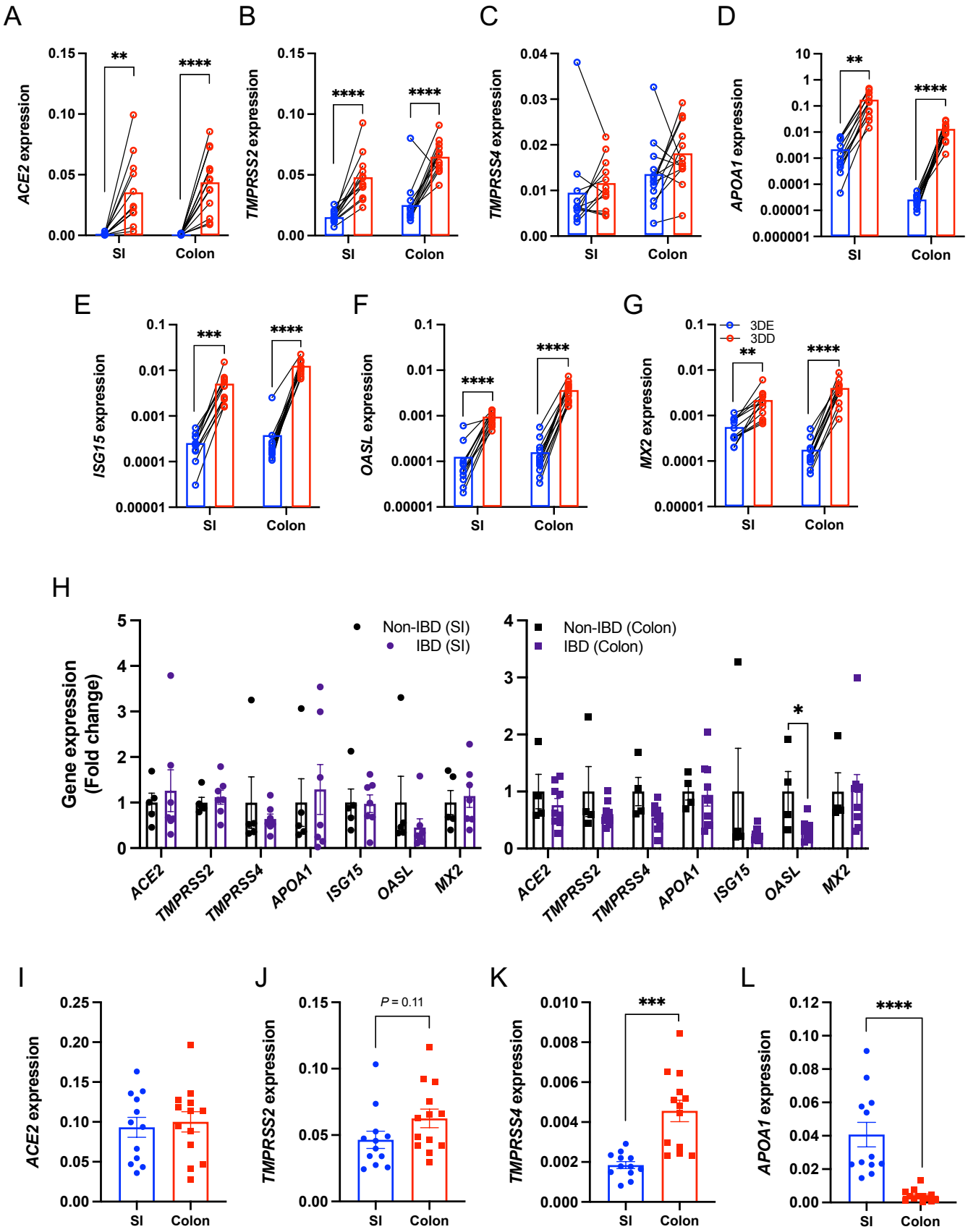
A
B
C
D
E
F
G
H
I
J
K
L
ACE2 expression
TMPRSS2 expression
TMPRSS4 expression
APOA1 expression
ISG15 expression
OASL expression
MX2 expression
SI
Colon
3DE
3DD
Non-IBD (SI)
IBD (SI)
Non-IBD (Colon)
IBD (Colon)
Gene expression (Fold change)
ACE2
TMPRSS2
TMPRSS4
APOA1
ISG15
OASL
MX2
P = 0.11

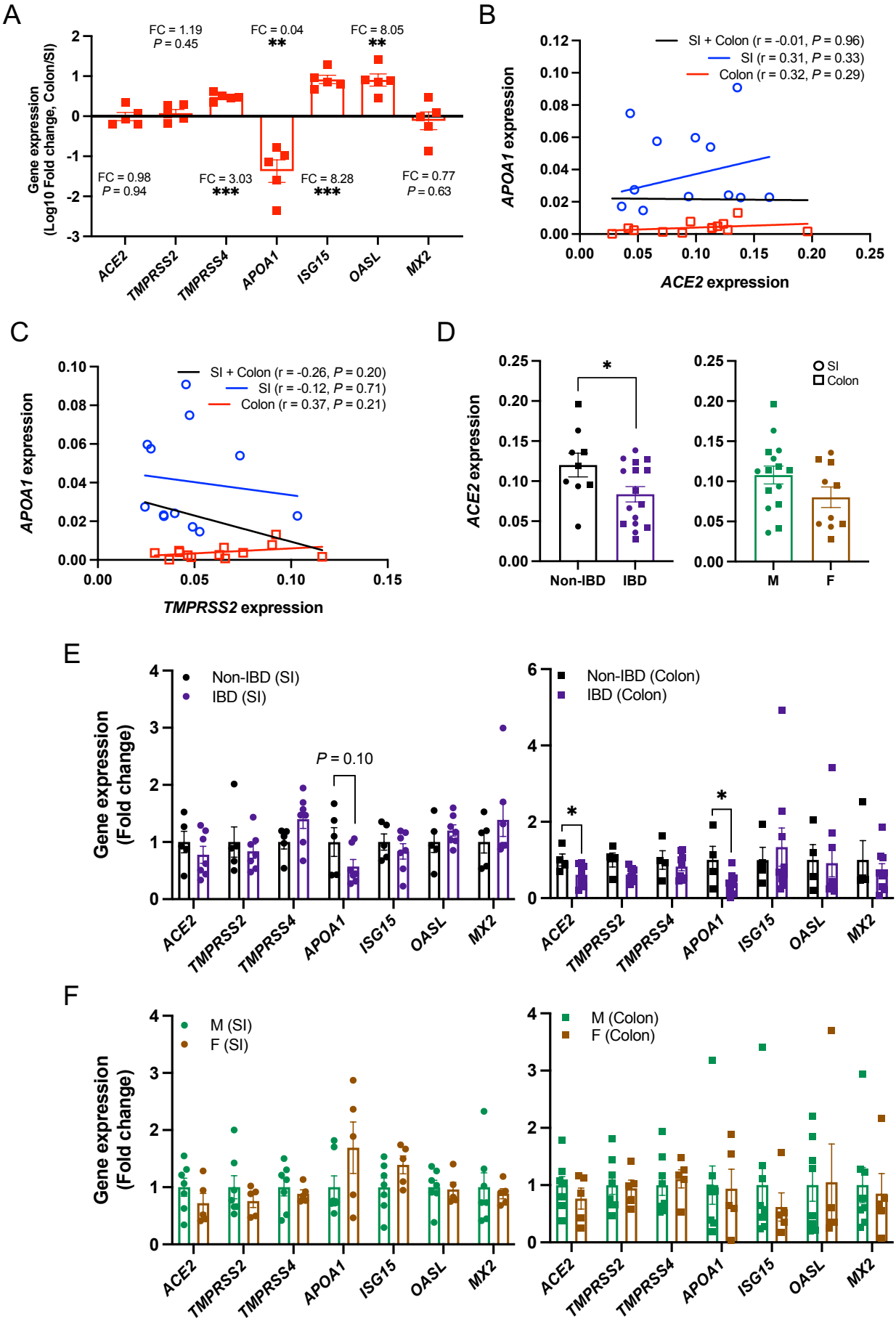
A
Gene expression (Log10 Fold change, Colon/SI)
FC = 0.98
P = 0.94
FC = 1.19
P = 0.45
FC = 3.03
***
FC = 0.04
**
FC = 8.28
***
FC = 8.05
**
FC = 0.77
P = 0.63
ACE2
TMPRSS2
TMPRSS4
APOA1
ISG15
OASL
MX2
B
SI + Colon (r = -0.01, P = 0.96)
SI (r = 0.31, P = 0.33)
Colon (r = 0.32, P = 0.29)
APOA1 expression
ACE2 expression
C
SI + Colon (r = -0.26, P = 0.20)
SI (r = -0.12, P = 0.71)
Colon (r = 0.37, P = 0.21)
APOA1 expression
TMPRSS2 expression
D
ACE2 expression
Non-IBD
IBD
SI
Colon
M
F
E
Non-IBD (SI)
IBD (SI)
P = 0.10
Non-IBD (Colon)
IBD (Colon)
Gene expression (Fold change)
F
M (SI)
F (SI)
M (Colon)
F (Colon)

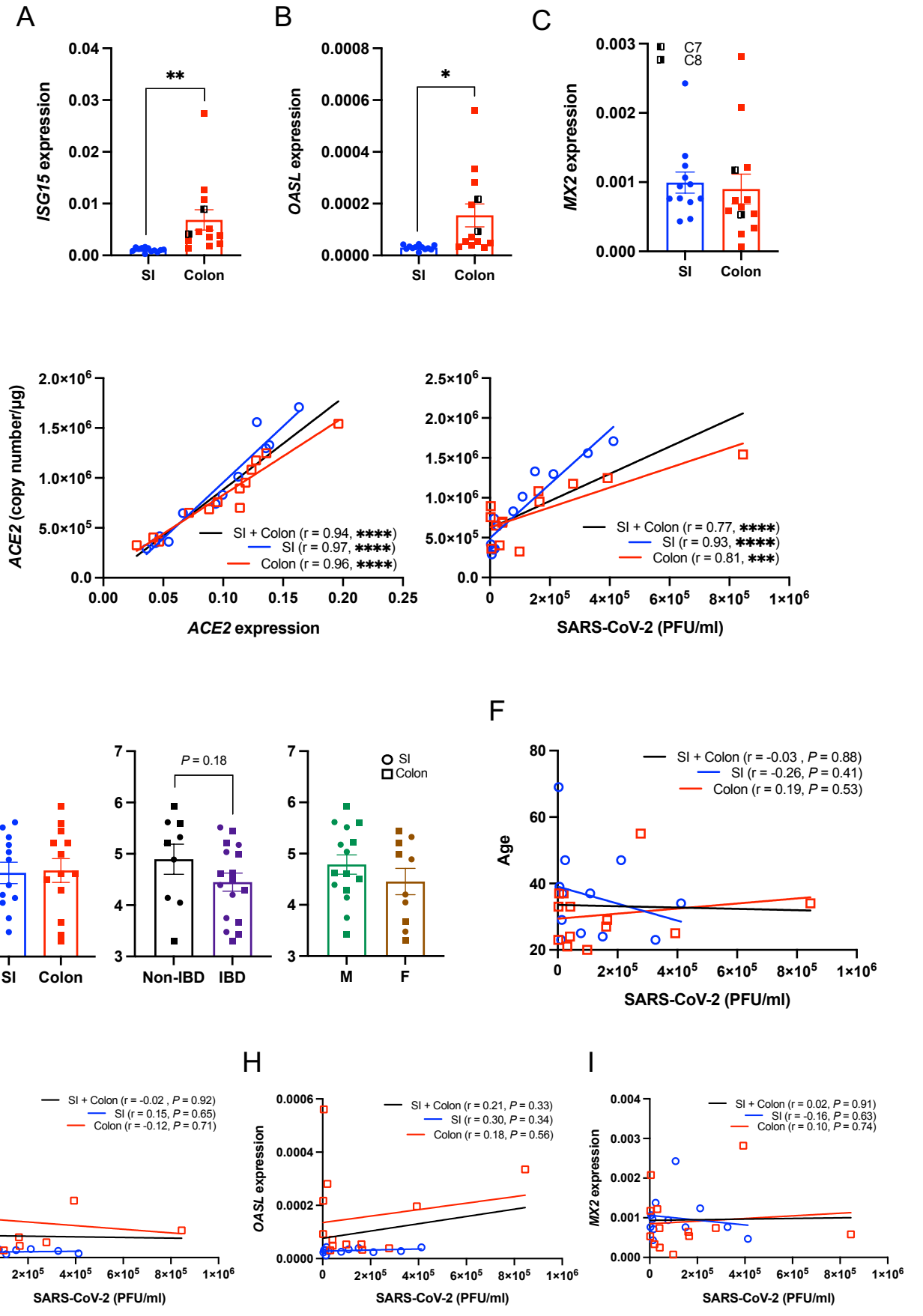
A
ISG15 expression
0.04
0.03
0.02
0.01
0.00
**
SI
Colon
B
OASL expression
0.0008
0.0006
0.0004
0.0002
0.0000
*
SI
Colon
C
MX2 expression
0.003
0.002
0.001
0.000
C7
C8
SI
Colon
D
ACE2 (copy number/μg)
2.0×10^6
1.5×10^6
1.0×10^6
5.0×10^5
0.0
0.00
0.05
0.10
0.15
0.20
0.25
ACE2 expression
SI + Colon (r = 0.94, ****)
SI (r = 0.97, ****)
Colon (r = 0.96, ****)
2.5×10^6
2.0×10^6
1.5×10^6
1.0×10^6
5.0×10^5
0.0
0
2×10^5
4×10^5
6×10^5
8×10^5
1×10^6
SARS-CoV-2 (PFU/ml)
SI + Colon (r = 0.77, ****)
SI (r = 0.93, ****)
Colon (r = 0.81, ***)
E
SARS-CoV-2 (Log10 PFU/ml)
7
6
5
4
3
SI
Colon
P = 0.18
Non-IBD
IBD
M
F
SI
Colon
F
Age
80
60
40
20
0
2×10^5
4×10^5
6×10^5
8×10^5
1×10^6
SARS-CoV-2 (PFU/ml)
SI + Colon (r = -0.03 , P = 0.88)
SI (r = -0.26, P = 0.41)
Colon (r = 0.19, P = 0.53)
G
ISG15 expression
0.03
0.02
0.01
0.00
SI + Colon (r = -0.02 , P = 0.92)
SI (r = 0.15, P = 0.65)
Colon (r = -0.12, P = 0.71)
0
2×10^5
4×10^5
6×10^5
8×10^5
1×10^6
SARS-CoV-2 (PFU/ml)
H
OASL expression
0.0006
0.0004
0.0002
0.0000
SI + Colon (r = 0.21, P = 0.33)
SI (r = 0.30, P = 0.34)
Colon (r = 0.18, P = 0.56)
0
2×10^5
4×10^5
6×10^5
8×10^5
1×10^6
SARS-CoV-2 (PFU/ml)
I
MX2 expression
0.004
0.003
0.002
0.001
0.000
SI + Colon (r = 0.02, P = 0.91)
SI (r = -0.16, P = 0.63)
Colon (r = 0.10, P = 0.74)
0
2×10^5
4×10^5
6×10^5
8×10^5
1×10^6
SARS-CoV-2 (PFU/ml)

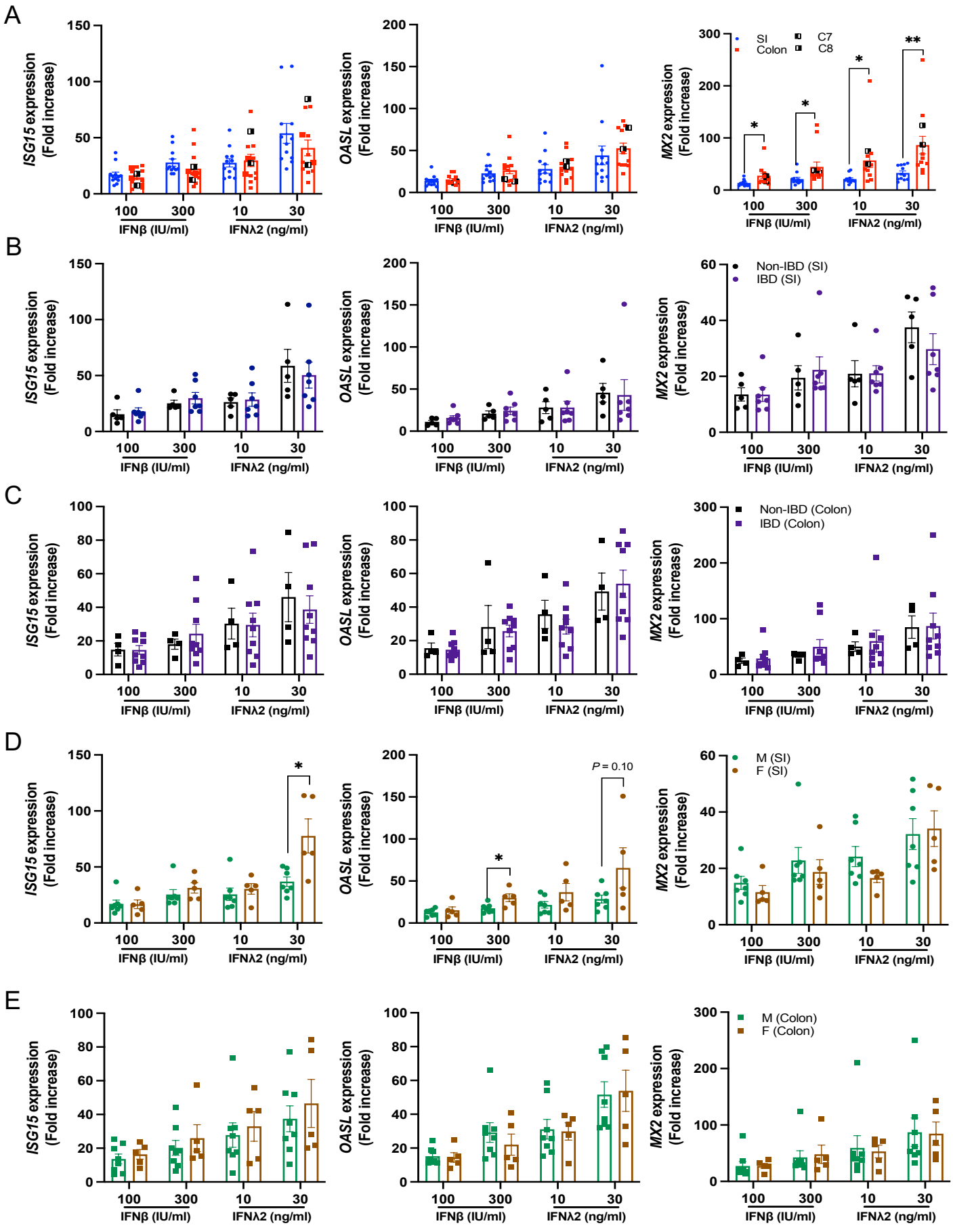
A
B
C
D
E
ISG15 expression (Fold increase)
OASL expression (Fold increase)
MX2 expression (Fold increase)
IFNβ (IU/ml)
IFNλ2 (ng/ml)
100
300
10
30
SI
Colon
C7
C8
Non-IBD (SI)
IBD (SI)
Non-IBD (Colon)
IBD (Colon)
M (SI)
F (SI)
M (Colon)
F (Colon)
P = 0.10

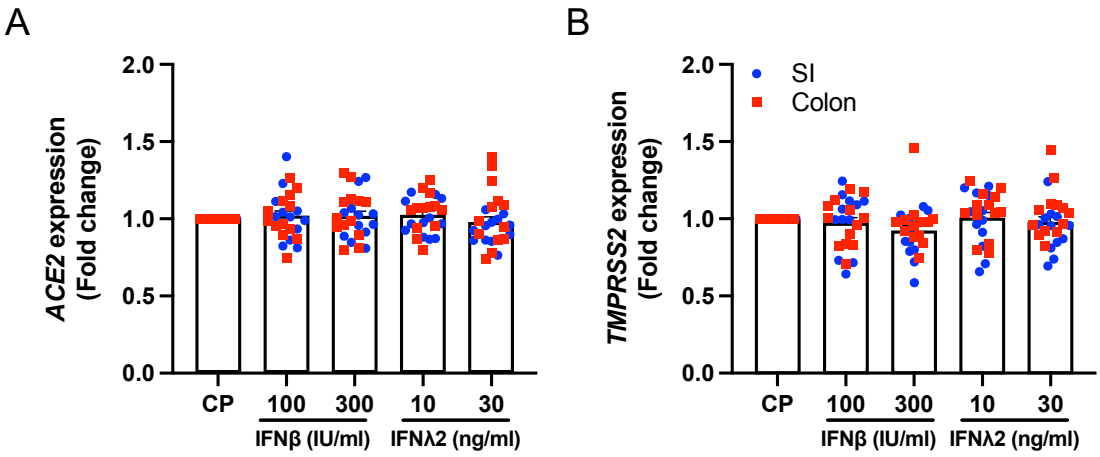
A
ACE2 expression
(Fold change)
2.0
1.5
1.0
0.5
0.0
CP
100
300
10
30
IFNβ (IU/ml)
IFNλ2 (ng/ml)
B
TMPRSS2 expression
(Fold change)
SI
Colon
2.0
1.5
1.0
0.5
0.0
CP
100
300
10
30
IFNβ (IU/ml)
IFNλ2 (ng/ml)

A

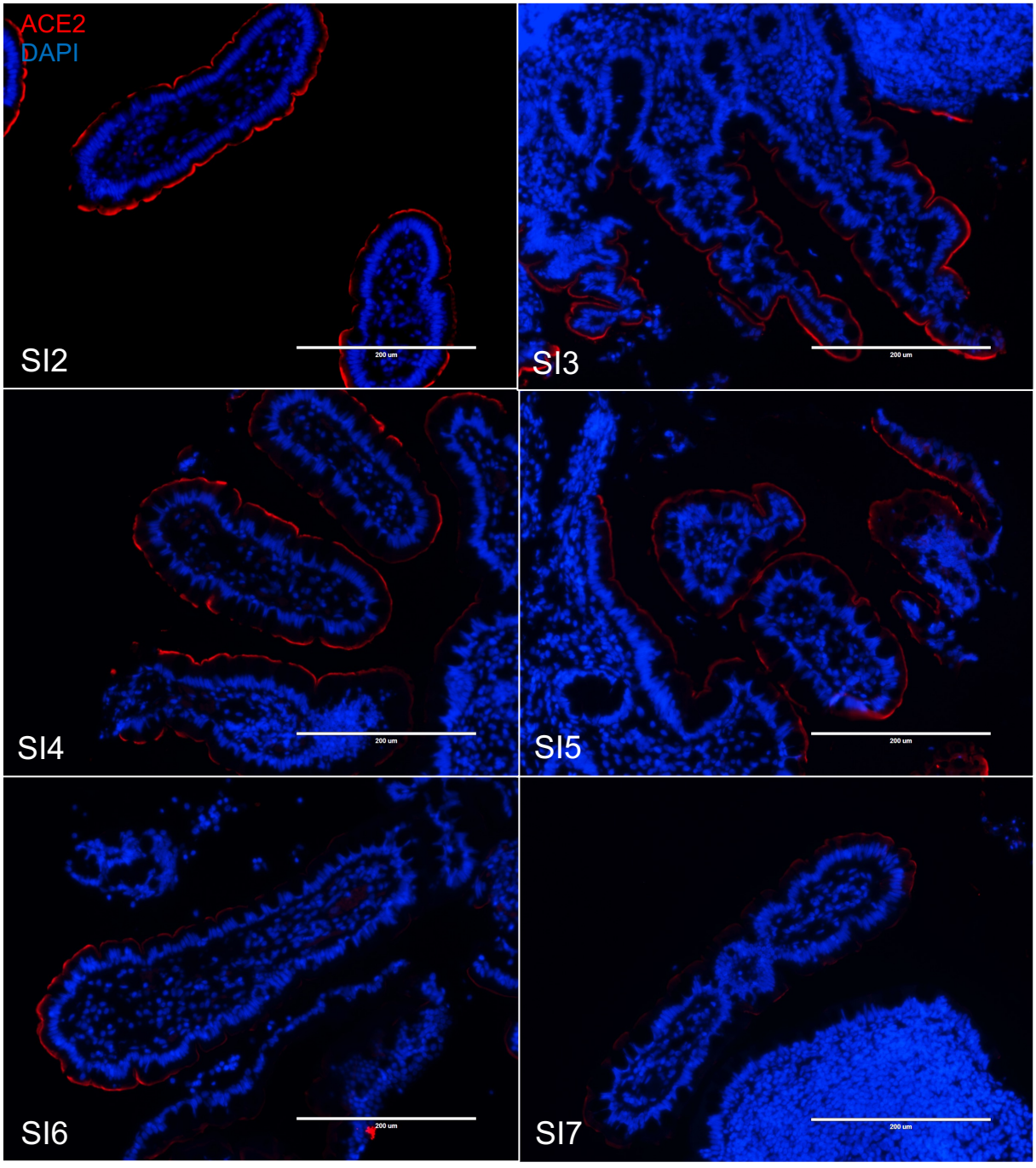

A

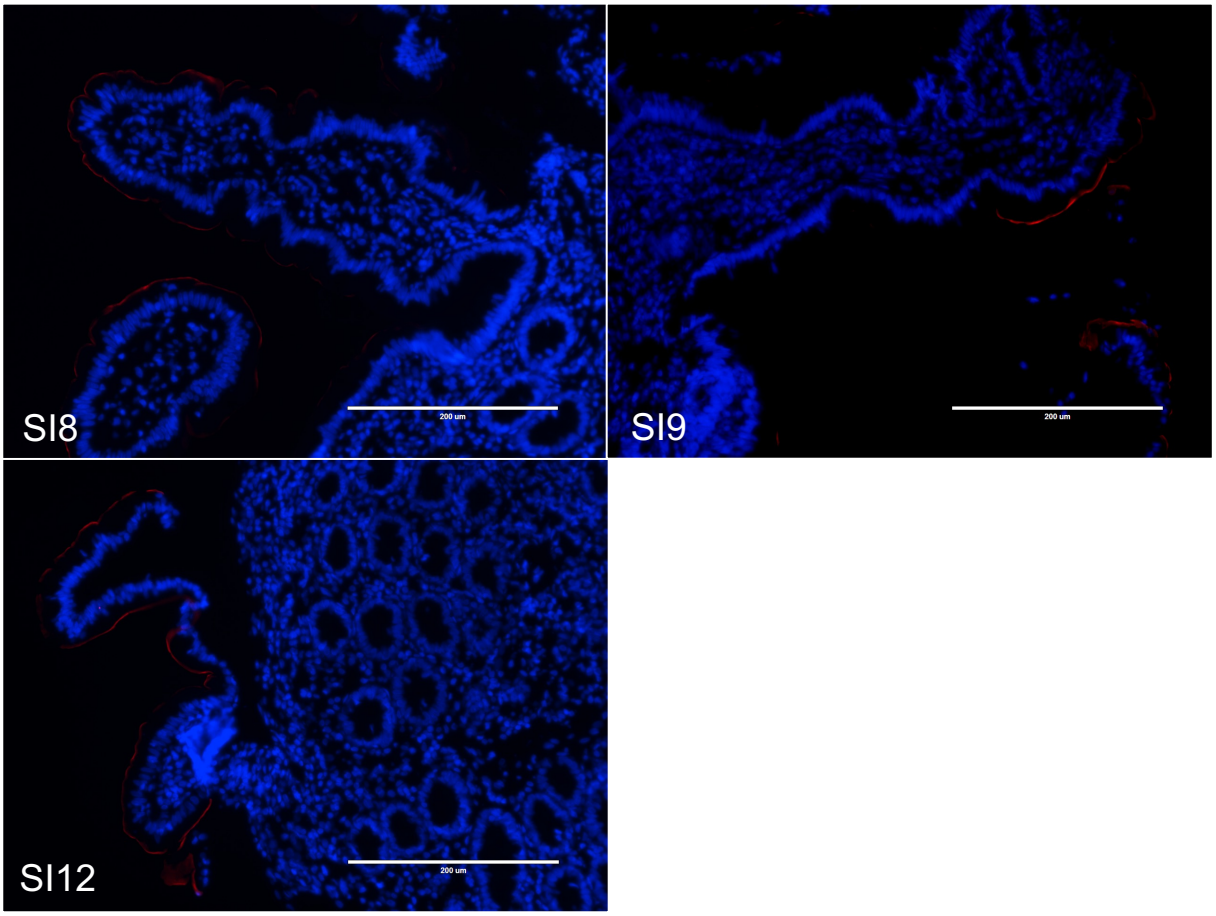
SI8
200 um
SI9
200 um
SI12
200 um

B

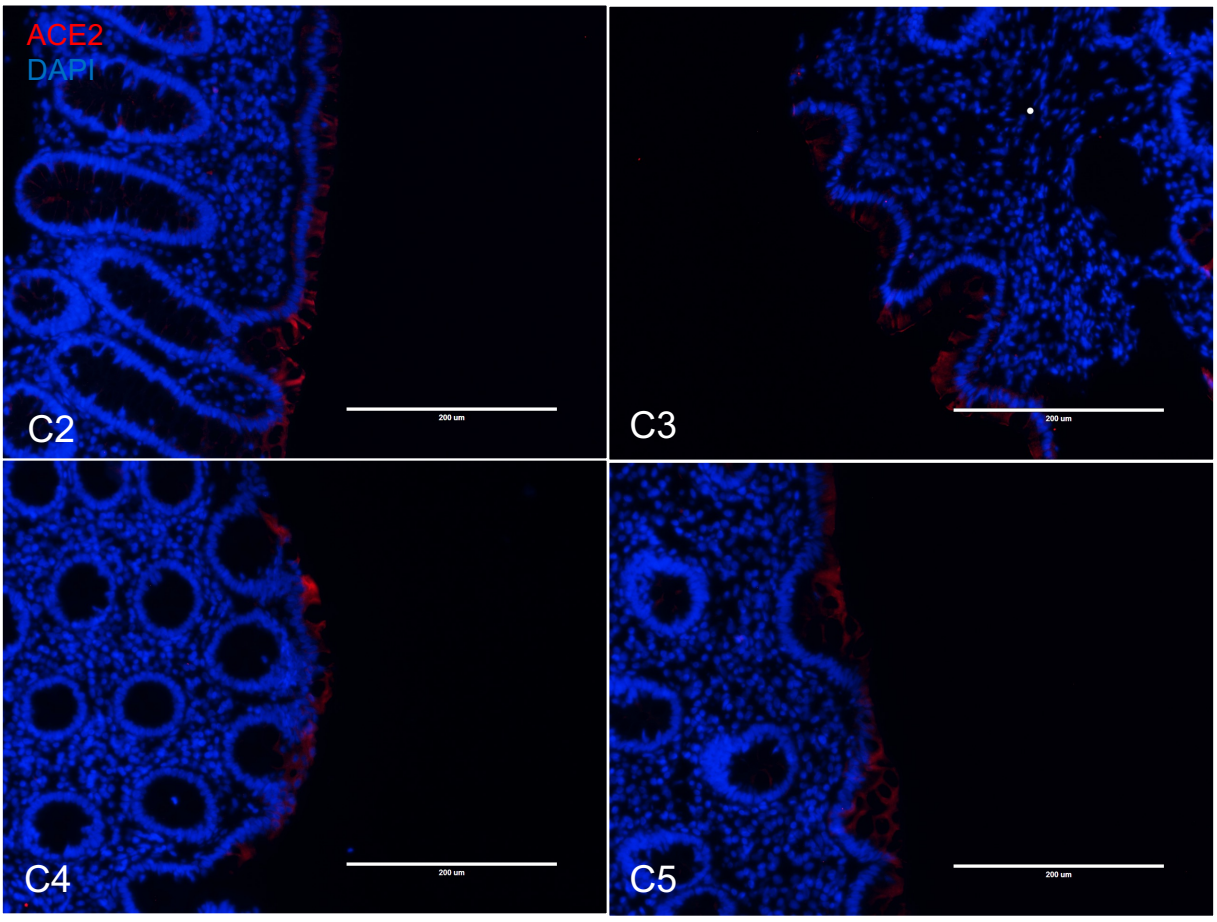
ACE2
DAPI
C2
200 um
C3
200 um
C4
200 um
C5
200 um

B

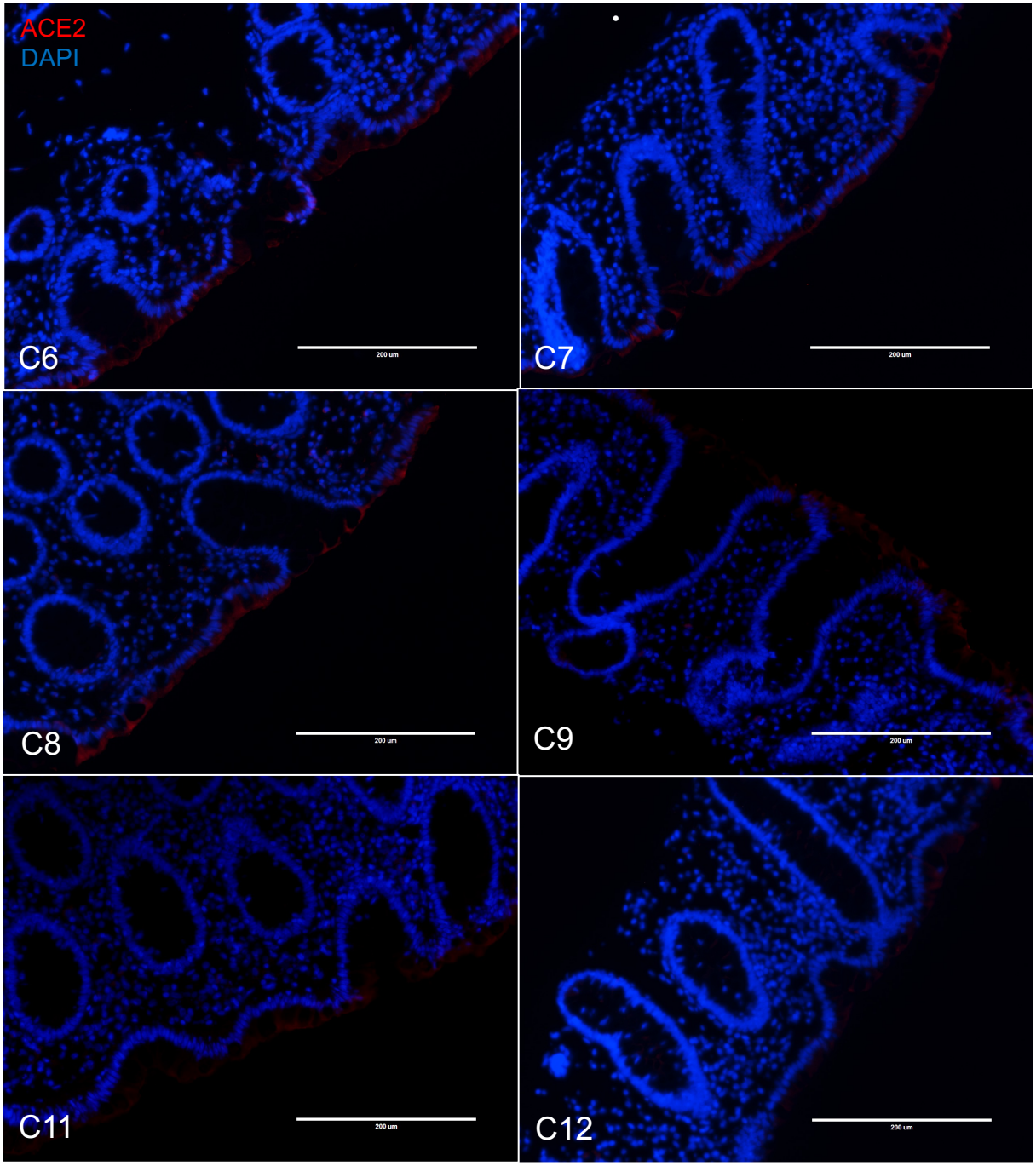
ACE2
DAPI
C6
200 um
C7
200 um
C8
200 um
C9
200 um
C11
200 um
C12
200 um

C

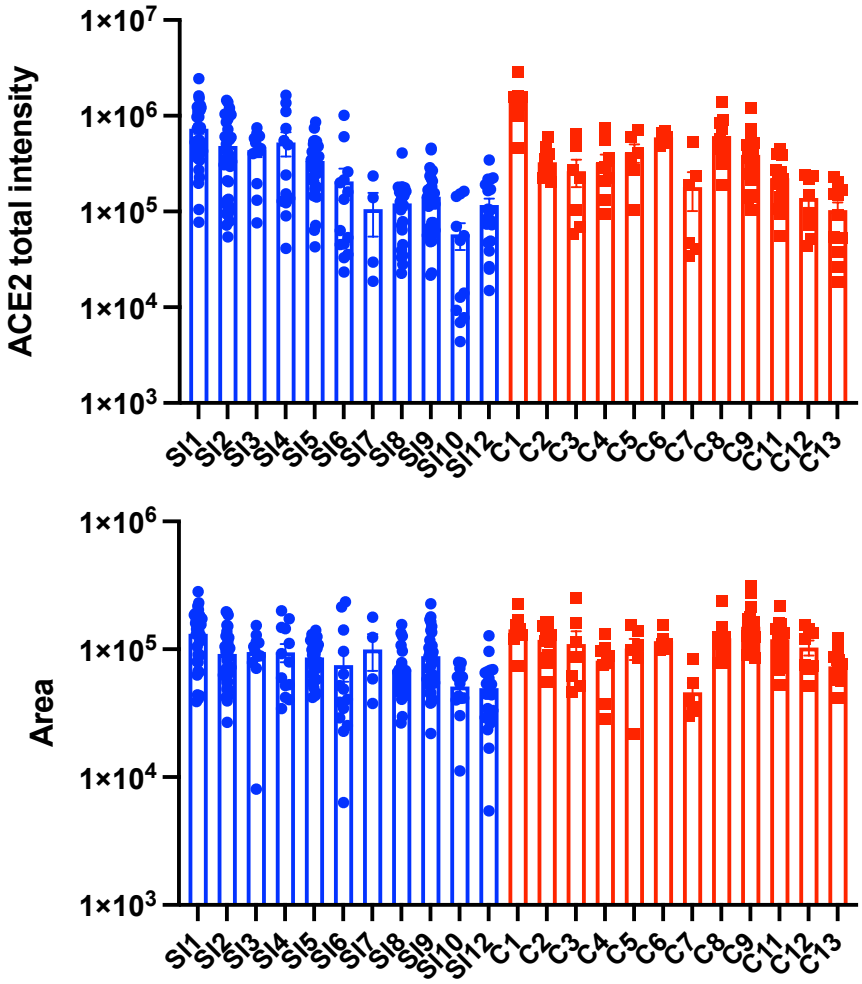
ACE2 total intensity
1×10^7
1×10^6
1×10^5
1×10^4
1×10^3
SI1 SI2 SI3 SI4 SI5 SI6 SI7 SI8 SI9 SI10 SI12 C1 C2 C3 C4 C5 C6 C7 C8 C9 C11 C12 C13
Area
1×10^6
1×10^5
1×10^4
1×10^3
SI1 SI2 SI3 SI4 SI5 SI6 SI7 SI8 SI9 SI10 SI12 C1 C2 C3 C4 C5 C6 C7 C8 C9 C11 C12 C13

A

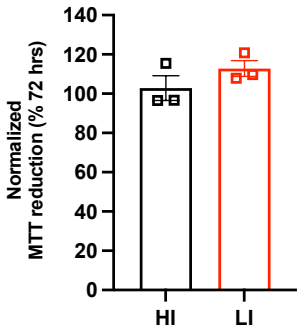

B

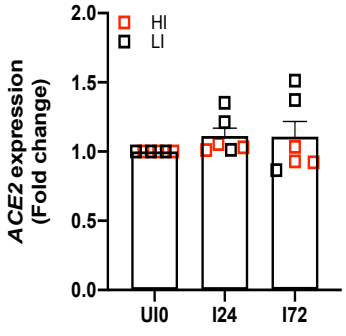

C

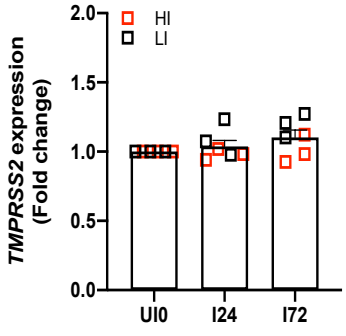

D

A vs B	Upregulated in	
	A	B
HI_UI0 vs LI_UI0	8	3
HI_UI72 vs LI_UI72	0	1
HI_I24 vs LI_I24	11	13
HI_I72 vs LI_I72	44	38
HI_UI0 vs HI_I24	10	3
HI_I24 vs HI_I72	12	180
HI_UI0 vs HI_UI72	0	0
HI_UI72 vs HI_I72	2	129
LI_UI0 vs LI_I24	7	0
LI_I24 vs LI_I72	46	207
LI_UI0 vs LI_UI72	0	0
LI_UI0 vs LI_I72	3	68

E

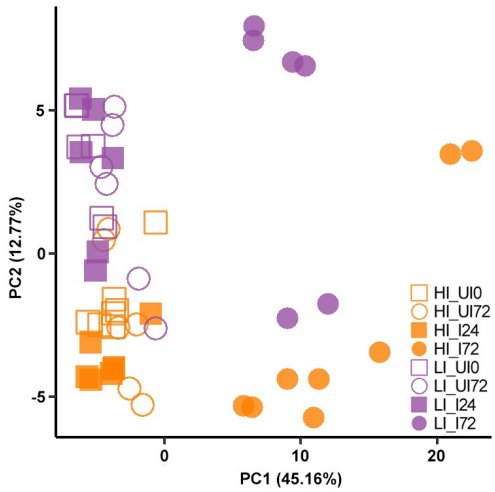

F

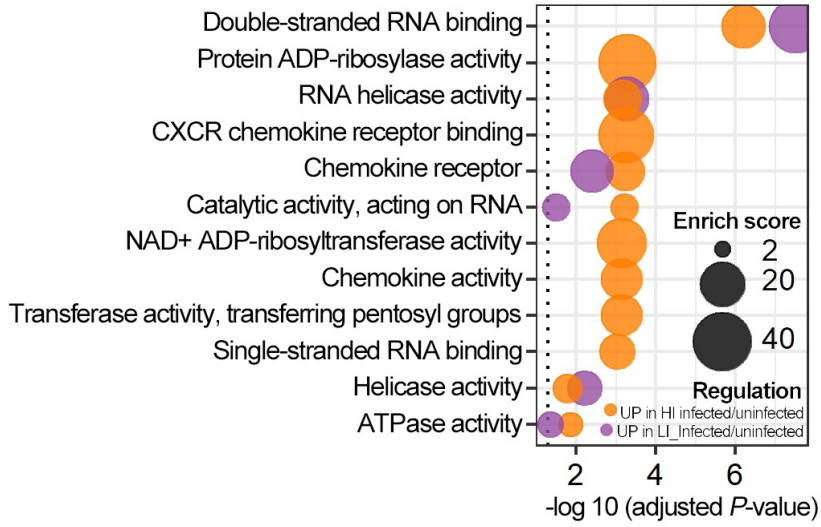

G

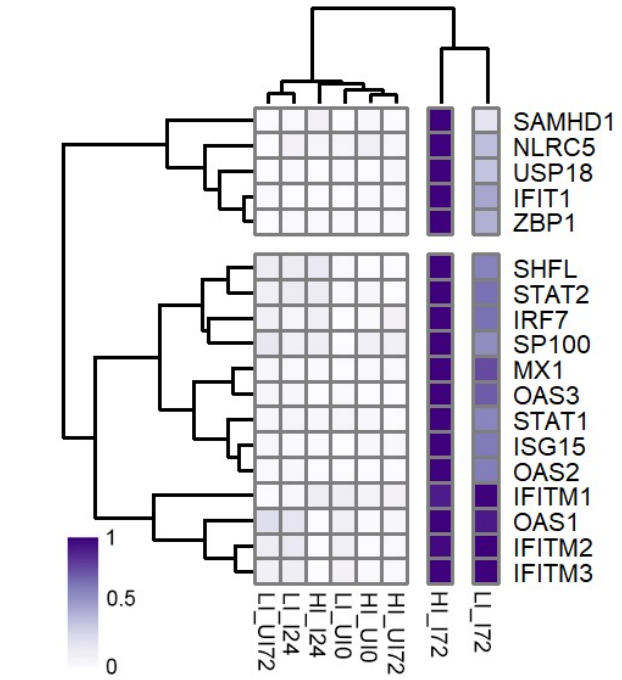

H

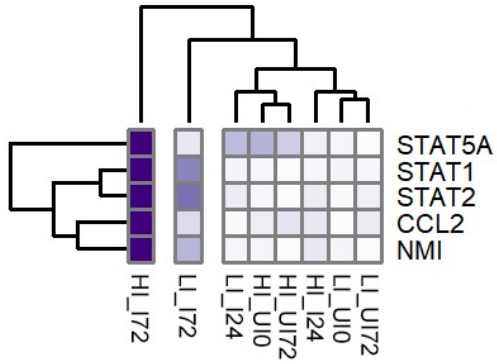

I

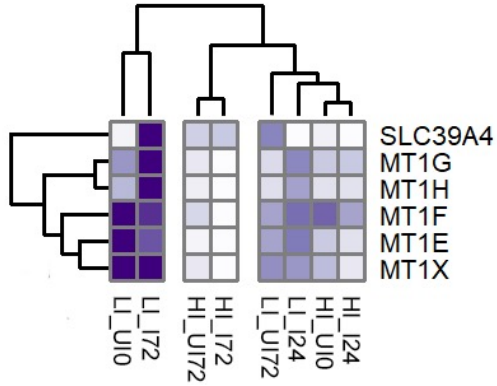

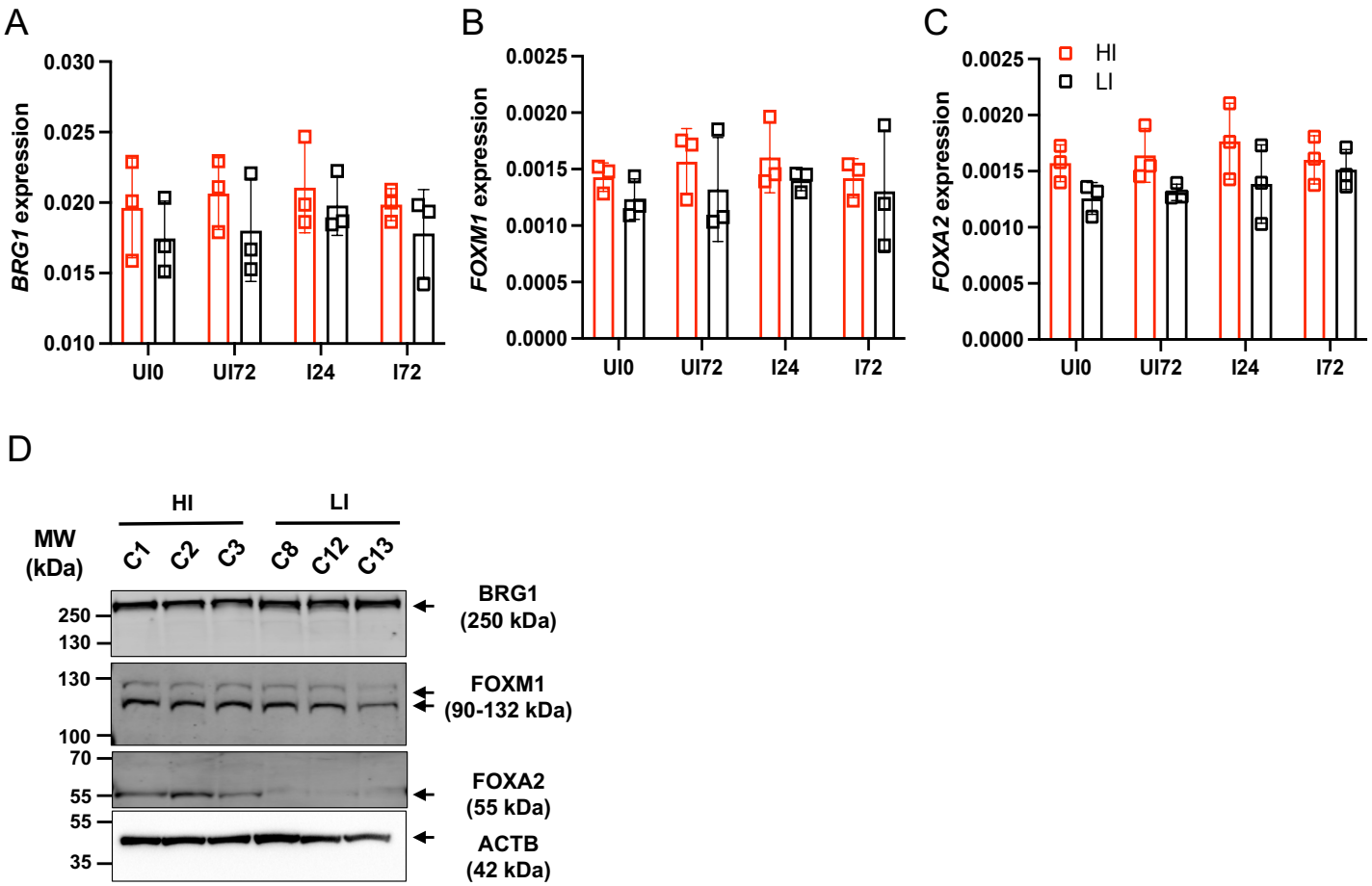
A
BRG1 expression
0.030
0.025
0.020
0.015
0.010
UI0
UI72
I24
I72
B
FOXM1 expression
0.0025
0.0020
0.0015
0.0010
0.0005
0.0000
UI0
UI72
I24
I72
C
FOXA2 expression
HI
LI
0.0025
0.0020
0.0015
0.0010
0.0005
0.0000
UI0
UI72
I24
I72

D
HI
LI
MW (kDa)
C1
C2
C3
C8
C12
C13
250
130
130
100
70
55
55
35
BRG1 (250 kDa)
FOXM1 (90-132 kDa)
FOXA2 (55 kDa)
ACTB (42 kDa)

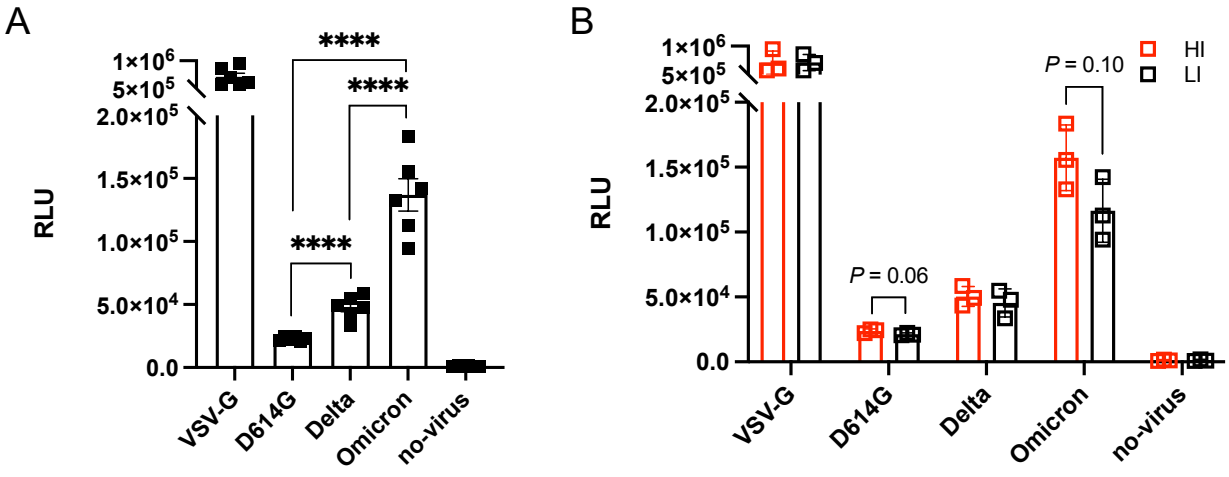
A
RLU
1×10^6
5×10^5
2.0×10^5
1.5×10^5
1.0×10^5
5.0×10^4
0.0
****
****
****
VSV-G
D614G
Delta
Omicron
no-virus
B
RLU
1×10^6
5×10^5
2.0×10^5
1.5×10^5
1.0×10^5
5.0×10^4
0.0
P = 0.06
P = 0.10
HI
LI
VSV-G
D614G
Delta
Omicron
no-virus